

Nanostructures in controlled thermonuclear fusion devices

V I Krauz, Yu V Martynenko, N Yu Svechnikov, V P Smirnov,
V G Stankevich, L N Khimchenko

DOI: 10.3367/UFNe.0180.201010c.1055

Contents

1. Introduction	1015
1.1 Development of a fusion reactor; 1.2 Influence exerted on the operation of fusion facilities by nanostructures formed therein; 1.3 Plasma-facing tokamak components and characteristics of the particle fluxes acting on them	
2. Erosion of tokamak components — the cause of nanostructure formation	1017
3. Nanostructured films in thermonuclear facilities	1018
3.1 Redeposition of erosion products; 3.2 Nanorelief of films; 3.3 Nanostructure of smooth films; 3.4 In-film hydrogen; 3.5 Theory of deposited-film relief formation; 3.6 Findings	
4. Dust: from nano- to micrometer-scaled dust	1030
4.1 Dust in tokamaks; 4.2 Dust production in model experiments; 4.3 Theory of dust formation; 4.4 Dust particles in plasma; 4.5 Plasma stabilization by dust injection; 4.6 Dust–surface interaction; 4.7 Findings	
5. Conclusion	1037
References	1037

Abstract. It is shown that the presence of nano-sized and nano-structured erosion products not only affects the operation of thermonuclear devices but also, to a large extent, determines the safety and economy of future thermonuclear reactors. The formation mechanisms and the characteristics and properties of deposited films and nano-sized dust that form in tokamaks are reviewed.

1. Introduction

1.1. Development of a fusion reactor

At present, when a start has been made on the construction of the International Thermonuclear Experimental Reactor (ITER) [1] and the development of the conception of the subsequent prototype commercial fusion reactor DEMO, the choice of materials for plasma-facing components and the problems of safety and reactor cost effectiveness are becoming progressively more topical. In this regard, it has become clear that dust and the nanostructured erosion products of tokamak materials are of paramount importance for the fusion reactor operation. We restrict ourselves to the consideration of a tokamak-based fusion reactor, since this area is the most advanced at the present time. This is the reason why investigations of dust and nanostructured films

are performed primarily in tokamaks or in tokamak-oriented simulation experiments. As this takes place, the operating conditions and requirements characteristic of ITER [2] are most frequently specified by way of example. Although nanostructured films and nano-sized dust are rather different objects, their roles are in many respects similar, and so for brevity's sake we shall use a common term — a nanostructure.

1.2 Influence exerted on the operation of fusion facilities by nanostructures formed therein

Typically, nanostructures formed due to the erosion of plasma-facing tokamak chamber elements play an adverse role. However, recently papers have appeared which propose that dust should be used to control the tokamak operation.

First, the nanostructures may be responsible for the capture and accumulation of tritium in a reactor, which is a problem both for reactor safety given the strength of tritium radioactivity, and for reactor energy efficiency due to the high cost of tritium (its price is around 10 mln USD per kilo). According to the ITER project, the tokamak should not accumulate more than 300 g of tritium [3].

Second, the nanostructures with a highly developed surface area are a hazard in emergencies related, in particular, to water inrush into the reactor chamber, as a catalyst for water decomposition and the production of an explosive amount of hydrogen [4].

Third, the radioactivity of dust is a hazard when opening the chamber [4].

The maximum admissible amounts of dust set for the ITER project are as follows: for carbon dust with a temperature $> 300^\circ\text{C}$, the admissible limit, according to the chemical activity requirement, is 6 kg; for tungsten dust according to radiation safety requirements it is 70 kg, and for beryllium dust it is 11 kg [5].

We shall show below the acuteness of the tritium accumulation problem as a result of tritium capture by the

V I Krauz, Yu V Martynenko, N Yu Svechnikov, V P Smirnov,
V G Stankevich, L N Khimchenko
Russian Research Centre 'Kurchatov Institute',
pl. Akademika Kurchatova 1, 123182 Moscow, Russian Federation
E-mail: martyn@nfi.kiae.ru, vsmirnov@kiae.ru

Received 22 March 2010, revised 16 April 2010
Uspekhi Fizicheskikh Nauk **180** (10) 1055–1080 (2010)
DOI: 10.3367/UFNr.0180.201010c.1055
Translated by E N Ragozin; edited by A Radzig

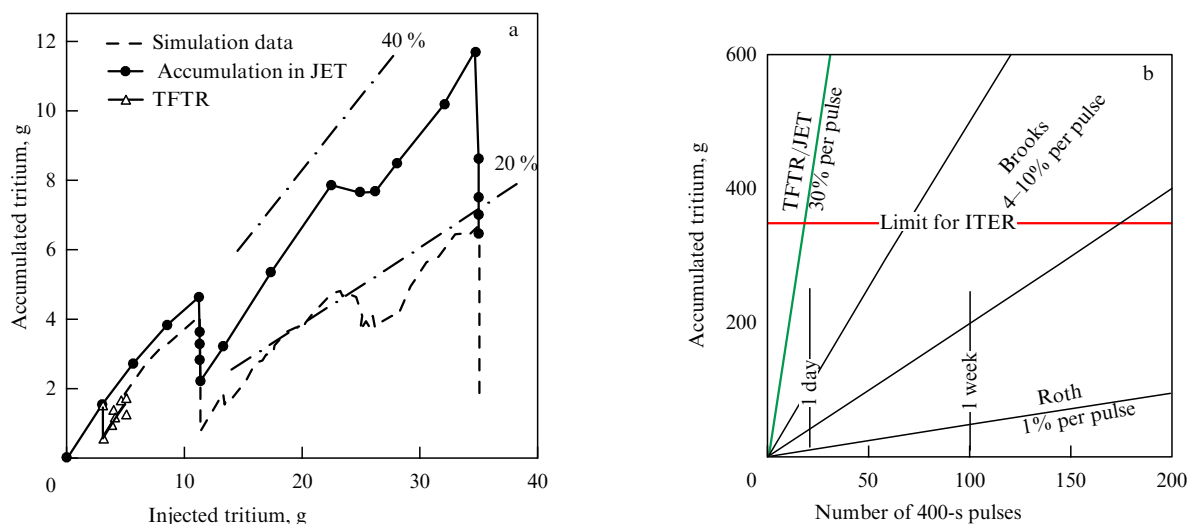


Figure 1. (a) Amount of accumulated tritium in the modern facilities as a function of its amount injected into the facility, and (b) amount of tritium accumulated in ITER as a function of the number of 400-s long pulses for different percentages of tritium confinement; Brooks predicts the accumulation of 4–10% of tritium per pulse, and Roth the accumulation of 1% per pulse. (Presentation of the International Tokamak Physics Activity group for the scrape-off-layer and divertor (SOL/divertor) plasmas.)

nanostructures at the chamber walls of modern facilities, as well as for ITER.

Figure 1 depicts the accumulation of tritium in modern facilities (Fig. 1a) [6] and its amount in relation to the number of pulses calculated for ITER at different tritium confinement percentages (Fig. 1b) [6]. The horizontal straight line indicates the admissible level of tritium in the chamber and is indicative of how often the chamber has to be cleaned. The data obtained on modern facilities testify to high percentages of the amount of tritium accumulated in tokamaks and to the absence of saturation in its accumulation. This is a demonstration that the tritium accumulation presents a highly significant problem. In the subsequent discussion we shall show that the tritium accumulation is directly related to material erosion products and their structure.

It is pertinent to note that the tritium accumulation in fusion reactor materials is difficult to study owing to its radioactivity and high cost, and therefore the bulk of research is performed on deuterium or hydrogen. Although isotopic effects do exist, for instance, the diffusion coefficient of hydrogen isotopes is inversely proportional to the square root of the isotope mass, $D \sim M^{-1/2}$, they have no pernicious influence on the gist of the findings arrived at.

1.3 Plasma-facing tokamak components and characteristics of the particle fluxes acting on them

Since the formation of dust and nanostructured films is associated with erosion, which is a problem in and of itself, at first we dwell on the mechanisms of erosion in tokamaks.

Figure 2a displays a section of the chamber of the ITER tokamak [7]. Its main plasma-facing components are the first wall (at the present time it is planned to make the first wall of beryllium, but replacing beryllium with tungsten is also possible) and the divertor located in the lower part of the ITER chamber (Fig. 2b). The principal task of the divertor is to remove the power of plasma streams, as well as helium, which is produced in the D, T reaction, and impurities from the principal chamber volume. This is achieved by configuring the magnetic field, whereby the outer magnetic lines of force extend to the divertor region. The domain in which

magnetic lines of force find themselves in the divertor region is referred to as the scrape-off layer (SOL). Magnetic surfaces in the inner part of the chamber are separated from the SOL by a separatrix — the surface with an intersection line [X-point is the intersection point (Fig. 2b)]. The removal of impurities and thermal fluxes from the main chamber is effected along the SOL lines of force.

At the initial stage, in the tritium-free operation with deuterium, the vertical plates of the ITER divertor will be fabricated of carbon fiber composite (CFC) (Fig. 2b), and at the next stage, when operating with deuterium and tritium, of tungsten (W). The remaining parts of the divertor will consist of tungsten.

According to the ITER project [1], the energy fluxes onto the first wall (i.e., the wall of the main tokamak chamber) will be equal to 5 MW m^{-2} during the working pulse, while the surface temperature of the plasma-facing wall will amount to 285°C in this case. The bulk of energy flux onto the first wall is brought by the plasma radiation, while the bombarding particles — fast neutral deuterium atoms produced in the charge exchange between plasma ions and neutral atoms of the gas evolved from the wall — are responsible for erosion. The atomic fluxes onto the first wall of ITER range from 10^{19} to $10^{21} \text{ m}^{-2} \text{ s}^{-1}$, and their energies vary from several electron-volts to several hundred electron-volts.

The energy fluxes incident on the divertor plates in the course of a working pulse are primarily due to SOL plasma fluxes; for ITER, the fluxes onto graphite plates, which carry the heaviest thermal load, will amount to 10 MW m^{-2} . In this case, the temperature will lie in the range between 460°C and 1280°C , depending on location at the plate. The fluxes of ions onto the ITER divertor plates will be equal to $10^{21} - 10^{22} \text{ m}^{-2} \text{ s}^{-1}$, and their energies to 5–100 eV.

Therefore, the operating conditions and the materials of various plasma-facing reactor components are different, and so their erosion is also different.

Apart from the influence of the above factors, which are caused by the presence of plasma, on the tokamak components, all tokamak materials will experience neutron irradiation. In fusion reactors, neutrons possess an energy of

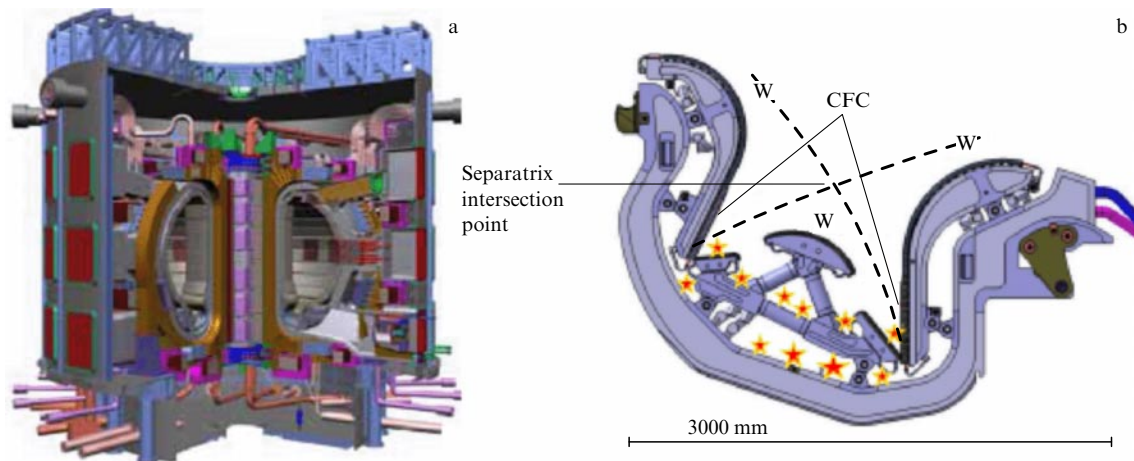


Figure 2. Sectional view of the ITER tokamak chamber (a) and divertor (b) located in the lower part of the ITER chamber; places of erosion product deposition are marked with the stars. At the first stage, ITER will operate on hydrogen and the divertor will have elements made of CFC material. It is planned that the second stage will involve operation on tritium and the divertor will consist only of tungsten.

14.1 MeV, while the energy of the neutrons in fission reactors is not substantially higher than 1 MeV. The fast neutron flux onto the first ITER wall will amount to $\sim 2 \times 10^{18} \text{ m}^{-2} \text{ s}^{-1}$. The neutrons are responsible primarily for the radiation damage in the volume of a material, but recent studies [8, 9] have shown that neutron-induced radiation damage may also exert an effect on the erosion of surfaces.

2. Erosion of tokamak components — the cause of nanostructure formation

Erosion in a tokamak is the source of atomic streams and of nano- and microparticle streams, which make up nanostructured films and dust particles ranging from several nanometers to several dozen micrometers in size [3]. Erosion processes in tokamaks are as follows:

- physical sputtering (by H isotopes and impurity atoms) as a result of bombardment of plasma-facing surfaces by ions and neutral atoms produced in a charge exchange process. This is the principal mechanism of erosion of the first wall proper. The sputtering gives rise to atomic streams from the surface into the wall plasma;
- blistering—the formation of gas bubbles due to hydrogen and helium accumulation in the surface layer, which is attended with the detachment of blister caps;
- chemical sputtering—material erosion resulting from the formation of volatile compounds of the material atoms and hydrogen isotopes. The chemical sputtering is most significant for graphite materials due to the formation of volatile CH_n hydrocarbons;
- radiation-enhanced sublimation of graphite—erosion at high temperatures ($> 100^\circ\text{C}$) under irradiation by accelerated ions or neutral atoms, also resulting in a stream of atoms into the wall plasma. However, the temperatures are not so high in normal regimes, and in off-nominal energy-intensive regimes the radiation-enhanced sublimation ranks below other erosion mechanisms in significance;
- erosion under the development of edge-localized modes (ELMs), i.e., pulse-periodic instabilities developing on the surface of the plasma column, and plasma disruptions consisting in the termination of the entire discharge, as well as when unipolar arcs ignite on the chamber walls. These regimes are attended with releases of a high amount of

power on the surface, and the surface temperature rises to several thousand degrees, with the effect that evaporation and droplet erosion for metals, as well as brittle fracture and nano- and microparticle emission for graphite, become the main erosion processes. Such erosion is most significant for divertor elements.

Significant plasma disruptions are relatively infrequent and may be surmountable events. ELMs, which permanently accompany the discharge operation, are believed to be the main cause of erosion of divertor plates and the source of dust particles in tokamaks. The ELM duration is on the order of 0.5 s, and an energy of $1\text{--}4 \text{ MJ m}^{-2}$ is released during this time. The duration of a plasma disruption is on the order of 1 s, and an energy of $20\text{--}40 \text{ MJ m}^{-2}$ may be released during this period.

Meanwhile, for the CFC divertor plates and under the development of ELMs with an energy release of 0.5 MJ m^{-2} , brittle fracture and the emission of dust particles set in after the occurrence of 100 ELM events, for 1 MJ m^{-2} —after 50 events, and for 1.5 MJ m^{-2} —after 10 events. The number of ELM events during one ITER discharge may range up to several hundred [10].

The melting of the edges of tungsten tiles, which make up the divertor components, takes place even under ELMs with an energy release of 0.6 MJ m^{-2} . The melting of the entire tungsten surface and the formation of bridges between the tiles take place for ELMs with a released energy density of 1.4 MJ m^{-2} . For ELMs with a power flux of 1.8 MJ m^{-2} , droplet erosion of tungsten shows its worth [11].

During the operation of a tokamak, many factors exert influence on the surfaces of its elements, resulting in the emergence of synergetic effects which complicate the study of erosion processes. The radiation-enhanced sublimation of graphite mentioned above is a manifestation of synergism. Another example of synergism may be provided by an increase in the H^+ -ion-induced sputtering coefficient for graphite [12] simultaneously irradiated by electrons with an energy of several hundred electron-volts, which do not produce sputtering by themselves.

In a thermonuclear reactor, the most important factor is neutron irradiation responsible for radiation damage. This damage affects not only the bulk material properties, but also the processes of surface erosion. Recently, a series of studies

[8, 9] was made to investigate the erosion of materials with radiation damage. A high level of radiation damage was achieved by cyclotron-accelerated fast ions (1–60 MeV) to model neutron irradiation. With this method, in several days of cyclotron operation it is possible to accumulate radiation damage equivalent to the damage produced under fast neutron irradiation up to a dose of 10^{22} neutrons per cm^2 . A study was made of carbon materials: pyrolytic graphite, MPG-8 graphite (Russian graphite), and SEP NB-31 carbon composite material (a candidate for an ITER material), as well as tungsten (99.95 wt.%). The carbon materials were irradiated by 5-MeV carbon ions, and tungsten was exposed to alpha particles with an energy of 3–4 MeV. Upon ion irradiation in the cyclotron, the materials under study with damage accumulated at a level of 0.1–10 displacements per atom (dpa) were exposed to the deuterium plasma in the ‘Lenta’ beam-plasma discharge facility for an ion energy of 100 eV for carbon materials, and 250 eV for tungsten, up to a dose of 10^{21} – 10^{22} ions per cm^2 . A manifold rise in the erosion coefficient was discovered for the carbon materials: a twofold rise for the SEP NB-31 composite, and a fivefold rise for pyrolytic graphite, which is supposedly related to the strong radiative swelling of these materials. Also discovered was a change in the surface structure of the tungsten upon ion irradiation in the cyclotron. The approach to the investigation of thermonuclear materials, developed in Refs [8, 9], which involves modeling neutron irradiation, appears to be important for the further study of the combined action of neutrons and plasma particles on the plasma-facing materials of fusion reactor elements.

Thus, it is valid to say that the main cause of surface erosion and the main ‘supplier’ of those erosion products which make up films and dust are ELMs and plasma disruptions.

3. Nanostructured films in thermonuclear facilities

3.1 Redeposition of erosion products

Erosion products emerging in one regions of the tokamak chamber are transferred to and deposited in other regions of the chamber. The general regularities in erosion product transfer are as follows: (i) transfer along magnetic lines of force and deposition in the divertor; (ii) deposition on the coolest surfaces (in particular, in the divertor lower part, as shown in Fig. 2b), and (iii) the tendency is observed for erosion product transfer from the tokamak outer part to the domain nearest to the tokamak vertical axis, referred to as the inner part. These regularities are not quite clearly defined. For instance, the outer part of the divertor in the Joint European Torus (JET) tokamak [13] accumulated 501 g of deposits, while the inner part accumulated 625 g. The same regularities are also observed in other tokamaks. Furthermore, the deposit distribution is not uniform: even on one divertor plate, the domains covered with films of erosion products are close to domains where erosion prevails (see Fig. 3). This supposedly results from the turbulence of streams.

3.2 Nanorelief of films

Various types of films form, depending on the deposition conditions—the discharge regime, the place of deposition, and the surface temperature. The formation of films of different types was observed in the T-10 tokamak, depending on the place of deposition and the discharge regime.

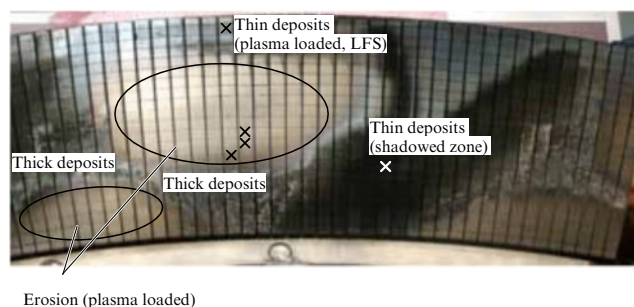


Figure 3. Domains of surface erosion and deposited films in the divertor of the French tokamak Tore Supra (LFS: low-field side).

The T-10 tokamak [14] comprises a toroidal chamber of a circular cross section, made of stainless steel with a major (minor) plasma radius of 1.5 (0.41) m, a toroidal magnetic field of up to 3 T, a plasma current of up to 0.5 MA, and a discharge pulse duration of up to 1 s; the working gas is deuterium. To limit the contact of hot plasma with the tokamak chamber, use is made of an annular diaphragm and a retractable graphite limiter sited on a small radius (0.3 m).

Away from the limiter, a smooth stratified film forms on the wall ($T_w \approx 50^\circ\text{C}$) in the regimes of discharge without limiter overheating ($T_{\text{lim}} \approx 300^\circ\text{C}$) (Fig. 4a). Close to the limiter but without its overheating, on the wall ($T_w \approx 50^\circ\text{C}$) there forms a globular film (Fig. 4b) consisting of smaller globules; the film relief resembles a cobblestone road, with no pores seen in this structure. The film deposited near the limiter in the regime with limiter heating up to $T_{\text{lim}} \approx 2000^\circ\text{C}$ is porous and looks like cauliflower (Fig. 4c). In the latter case, the film was deposited on the surface with a temperature $T_w \approx 100^\circ\text{C}$ [15].

Films with a developed relief were also observed in the JT-60U, TEXTOR (Tokamak Experiment for Technology Oriented Research), and JET tokamaks, in the LHD (Large Helical Device) stellarator, in the NAGDIS-II (Nagoya Divertor Simulator) linear plasma facility, and in other fusion facilities (Fig. 5). Here, several kinds of films were revealed: globular [16], cauliflower-like [16, 17], ovoid-shaped [18], stratified [19], and columnar [18].

In the majority of cases, the films with a developed relief have several hierarchic levels of granules. Large granules consist of smaller elements, which in turn consist of even smaller ones. The dependence of the number of granules $N_i(r_i)$ on their size r_i has the form $N_i(r) \sim r_i^{-d}$, which is characteristic of a fractal structure. The $N(r)$ dependence is plotted on the lg–lg scale in Fig. 6 for a cauliflower-like film from the T-10 tokamak. The resultant fractal dimension is $d = \partial \lg N_i / \partial \lg r_i = 2.2$. For the majority of films investigated, it was found that $d = 2.2 \pm 0.2$ [22].

The fractal structure of the film relief was also obtained in modeling the ELM action on tungsten in a quasistationary high-current plasma accelerator (QHCPA) (with a power flux of 1–1.5 MJ m^{-2} , and a pulse duration of 0.5 ms; the samples were exposed to ≈ 100 pulses) [23]. In this case, the fractal dimension of the film was also $d = 2.2$. It is noteworthy that the surface of the tungsten film produced in these experiments contains a substantially larger amount of impurities (C, O, Ca, Fe, Cr, Cu) than its in-depth layers. There is a notion that impurities contribute to the formation of a developed fractal structure in films.

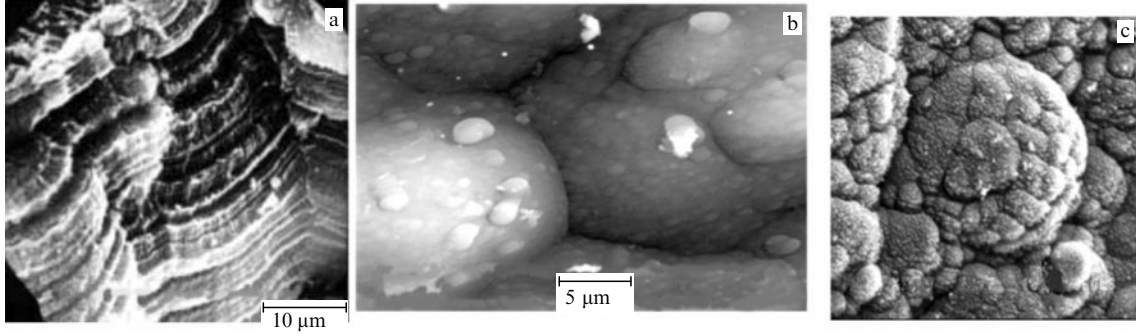


Figure 4. Films deposited in the T-10 tokamak: (a) stratified film away from the diaphragm; (b) globular film near the diaphragm, and (c) globular film near the diaphragm with the limiter heated up to $T_{\text{lim}} \approx 2000^\circ\text{C}$.

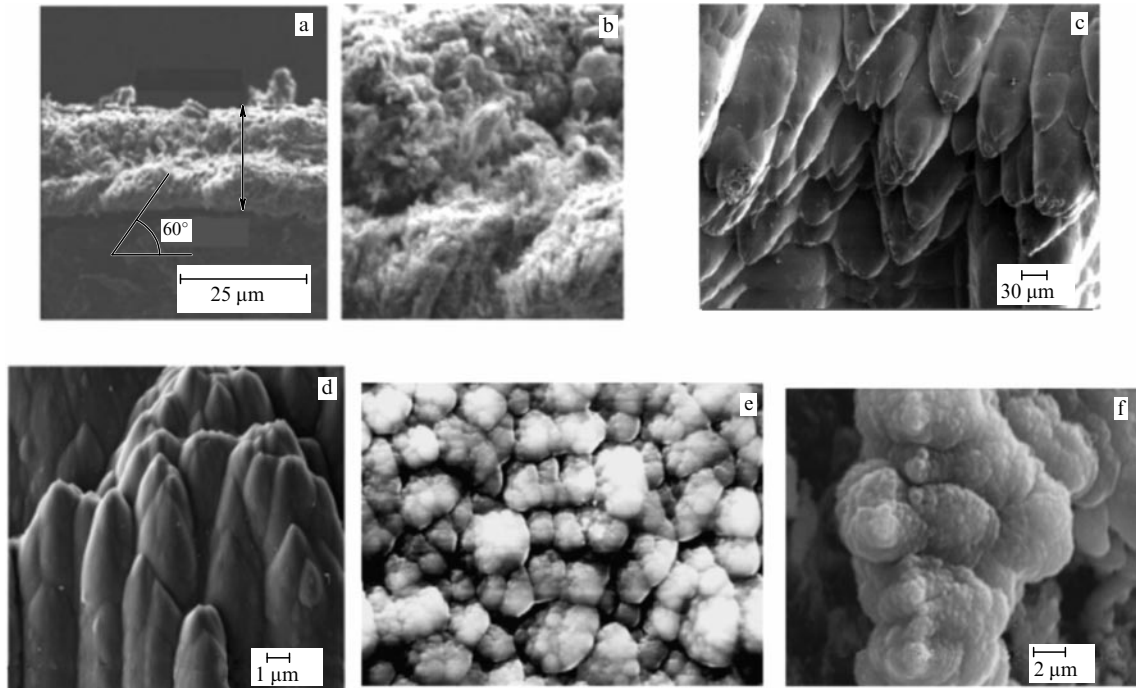


Figure 5. Structures of films deposited in tokamaks: (a, b) Japanese JT-60U tokamak [20], (c) French Tore Supra tokamak [18], (d) German TEXTOR [21], (e) DOE's DIII-D, and (f) NAGDIS II linear machine [17].

Of fundamental importance is the question of what the minimal size of granules is in the film fractal structure, because it is the minimal granule size that determines the specific surface area (SSA) of the films and thereby their adsorption capacity and chemical activity. The SSA of a fractal surface with a size distribution of granules $N_i(r) \sim r_i^{-d}$ is expressed as

$$\text{SSA} = \frac{S_0}{\rho V} = \frac{\int A r^{-\alpha} 4\pi a_0^2 (r/a_0)^d dr}{\rho \int A r^{-\alpha} 4/3\pi a_0^3 (r/a_0)^d dr} = \frac{3}{\rho a_0}, \quad (1)$$

where ρ is the film material density, A and α are constants in the size distribution of particles $f(r) = A r^{-\alpha}$, and a_0 is the minimal cluster size in the hierarchy.

It has been possible to determine the minimal granule size owing to the use of scanning probe microscopy, which was first applied to investigate the films of the T-10 tokamak in the Nuclear Fusion Institute (NFI) of the Russian Research Centre 'Kurchatov Institute' (RRC KI). In particular, use is made of a specially designed miniature scanning tunneling microscope placed into the T-10 tokamak chamber. The relief

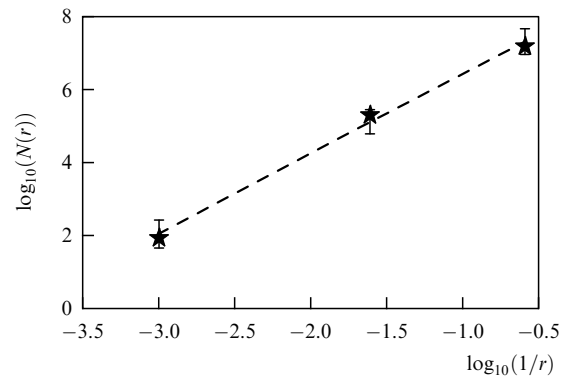


Figure 6. Estimate of the fractal dimension of the film from the T-10 tokamak. Dependence of $N(r)$ on $1/r$ plotted on the lg–lg scale.

of the film growing in the T-10 tokamak is scanned on the intervals between plasma discharge pulses, making it possible to follow the film growth after every pulse.

The minimal structure dimension revealed by scanning probe microscopy is equal to ≈ 15 nm [23], which corresponds to $SSA \approx 170$ m² g⁻¹ for carbon, and to ≈ 16 m² g⁻¹ for tungsten. For comparison we note that the specific surface area of the hydrocarbon film extracted from the Tore Supra tokamak amounts to $SSA = 180$ m² g⁻¹, which was measured by the Brunauer–Emmett–Teller (BET) method from methane adsorption [18]. The proximity of the SSA values for T-10 and Tore Supra is indicative of the universality of the film growth mechanism in tokamaks.

The film growth rate in tokamaks with a divertor ranges from 1.5 nm s⁻¹ to 12 nm s⁻¹ [3]. In the T-10 tokamak, films with a thickness of up to 10–50 μ m formed after approximately 1000 discharge pulses with a duration of ≈ 1 s.

The deposited layer formation was most clearly traced in experiments by Guseva et al. [24], which modeled the conditions of film deposition in tokamaks. The film was produced by simultaneous deposition of 300-eV C₂H₂⁺ ions with an ion flux density of 10²¹ m⁻² s⁻¹ and carbon atoms — the products of graphite sputtering in a stationary regime. The deposition was effected on tungsten and graphite samples at a temperature of 670 K. The structure of the films co-deposited on tungsten varied from smooth and uniform for small irradiation doses ($\leq 1 \times 10^{23}$ m⁻²) to globular for large ones (10^{24} m⁻²) (Fig. 7). On graphite, films with a globular structure are formed even for an irradiation dose of 2×10^{23} m⁻². The globular film formation takes place by way of nucleation of individual small globules and a gradual increase in their density and size. The film density amounts to 0.52 and 0.79 of the initial graphite density for the uniform and globular structures, respectively. The density of the smooth uniform films is lower because the fraction of hydrogen is higher in these films (this issue will be discussed in Section 3.4).

The above-mentioned experiments revealed the following.

(1) Smooth films are produced for small irradiation doses (10^{23} m⁻²).

(2) As the dose increases (to 4×10^{23} m⁻²), islands-clusters form on the sample surface.

(3) For high doses (10^{24} m⁻²), a developed film relief emerges.

(4) The development of a relief is substrate-dependent (Figs 7c and 7d).

3.3 Nanostructure of smooth films

Smooth films constitute the main accumulator of hydrogen isotopes. The films collected from the wall of the vacuum chamber of the T-10 tokamak were studied at the Kurchatov Center for Synchrotron Radiation and Nanotechnology of RRC KI using a wide variety of techniques, which comprised the following main areas:

— powder X-ray diffraction (XRD) and small-angle X-ray scattering (SAXS) using the synchrotron radiation (SR) of the Sibir-2 storage ring;

— optical spectroscopy and luminescence;

— infrared (IR) spectroscopy;

— Raman spectroscopy (RS);

— X-ray absorption [extended X-ray absorption fine structure (EXAFS), and near-edge extended X-ray absorption fine structure (NEXAFS)];

— thermal desorption spectroscopy (TDS);

— X-ray fluorescence (XRF) analysis with the use of synchrotron radiation;

— electron paramagnetic resonance (EPR);

— volt–ampere characteristics (VACs).

Investigations were made of smooth uniform films, i.e., ‘flakes’, mostly goldish in color, from the T-10 tokamak (2002 campaign, films collected near the limiter and the annular diaphragm of MPG-8 graphite). These carbon films have a high relative content of deuterium and protium, namely, an

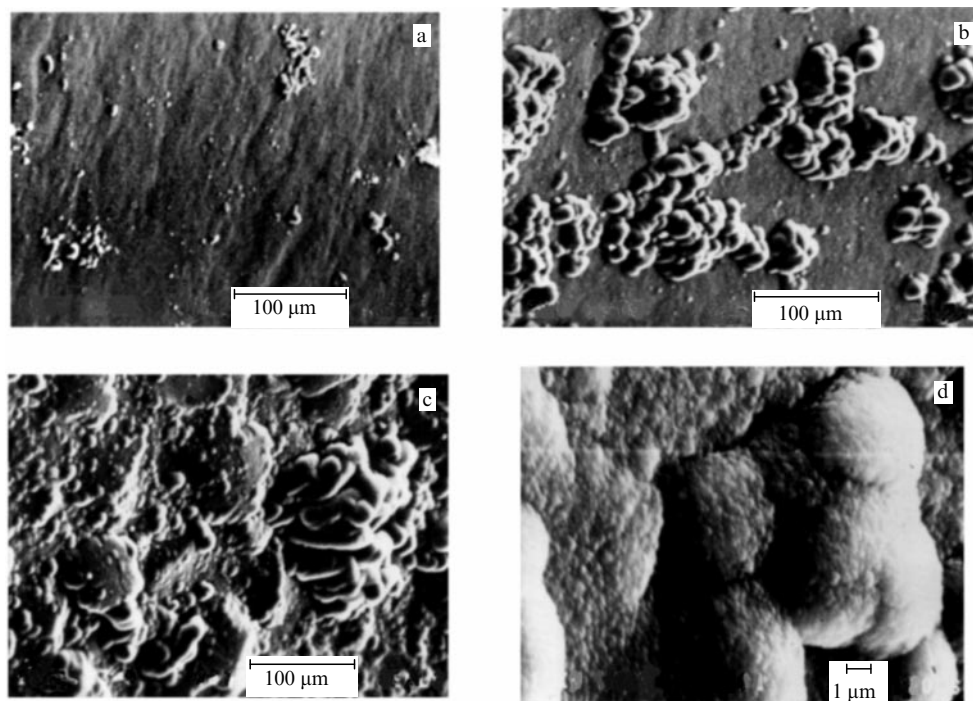


Figure 7. Typical microphotographs of the surface of co-deposited layers on tungsten for various irradiation doses: (a) 10^{23} m⁻², (b) 4×10^{23} m⁻², and (c) 10^{24} m⁻², as well as on MPG-8 graphite (d) for an irradiation dose of 2×10^{23} m⁻².

atomic ratio $D/C \approx 0.5-0.8$ ($H/C \approx 0.2-0.3$). The highest ratio $D/C \approx 1.4$ was obtained for semitransparent rich yellow films whose color is due to their wide forbidden band E_g . In darker films, the energy gap width is narrower and the relative content $D/C = 0.2-0.4$. The darker films are produced at higher temperatures.

The flakes are 20–30 μm in thickness, and about 0.5 cm^2 in size. They are slightly curved owing to the stress which arises with increase in the film thickness in the tokamak, i.e., the concave side faces the plasma (hereinafter referred to as the plasma side), while the convex side faces the chamber wall (the wall side).

Below we shall present the main experimental evidences concerning the investigation of these films, which testify to the presence of a variety of nanodimensional structure elements in films with a smooth relief.

By means of X-ray fluorescence analysis with the use of synchrotron radiation (XRFA-SR), Svechnikov et al. [25] discovered 12 microimpurities, primarily of 3d, 4d, and 5d transition metals: Fe, Mo, Cr, Ni, Ti, and some others, with relative concentrations of 50–7000 ppm and a total concentration of 1.5%. In this case, almost one half of the impurities are due to Fe atoms. This circumstance is also confirmed by EPR data (9.9 GHz, 6000 G, 300 K) obtained from high-concentration paramagnetic impurities, as shown below.

The majority of microimpurities emerge in the surface erosion of the T-10 vacuum chamber made of 03Kh17N14M3 stainless steel. Furthermore, microimpurities of metals, on the order of a few tenths of a percent, also present in the sputtered MPG-8 graphite, of which the limiter and the annular diaphragm are made. In this case, the elements Fe, Ni, Ti, Mo, Nb, and Cr may, in principle, form carbides Fe_3C , Ni_3C , TiC , MoC , NbC , and CrC . For the Fe microimpurity, which has the highest relative concentration, this possibility was revealed proceeding from the analysis of EXAFS spectra for the Fe K -edge in Ref. [26]. The authors of the latter work measured the Fe–C distance at 0.211 nm and found the coordination number equal to 6.2, i.e., Fe cations supposedly occupy octahedral positions surrounded by six C atoms. The average Fe–C distance turned out to be rather close to the corresponding distance in iron carbide Fe_3C ; however, the features of distant coordination Fe–Fe spheres are missing. Therefore, this is indicative of the presence of Me–C clusters in the film, which are located in the hydrocarbon $\text{sp}^3 + \text{sp}^2$ CH, CD matrix. Its composition is inferred from the vibrational structure obtained from the IR spectra given in Fig. 12 (see Section 3.4.).

The X-ray diffraction structure and the small-angle X-ray scattering spectra of the films are plotted in Fig. 8. The X-ray diffraction spectrum (Fig. 8a) recorded in Debye–Scherrer transmission geometry at a wavelength $\lambda = 0.1072$ nm, which was obtained with the Sibir-2 synchrotron radiation source (at the Structural Materials Science (SMS) end-station) of the Kurchatov Center for Synchrotron Radiation and Nanotechnology (KCSRNT), consists of two broad peaks corresponding to interplanar spacings of 0.7 and 0.23 nm. These data correlate with the findings of Svechnikov et al. [27], who measured the interplanar spacings at 0.77 and 0.28 nm using an X-ray tube technique.

The large width of the peaks in Fig. 8a is indicative of the presence of an amorphous structure, i.e., a structure different from the crystal structure of graphite with its narrow lines. It is well known that the most intense line of graphite, which is the structural prototype for the majority of carbon materials

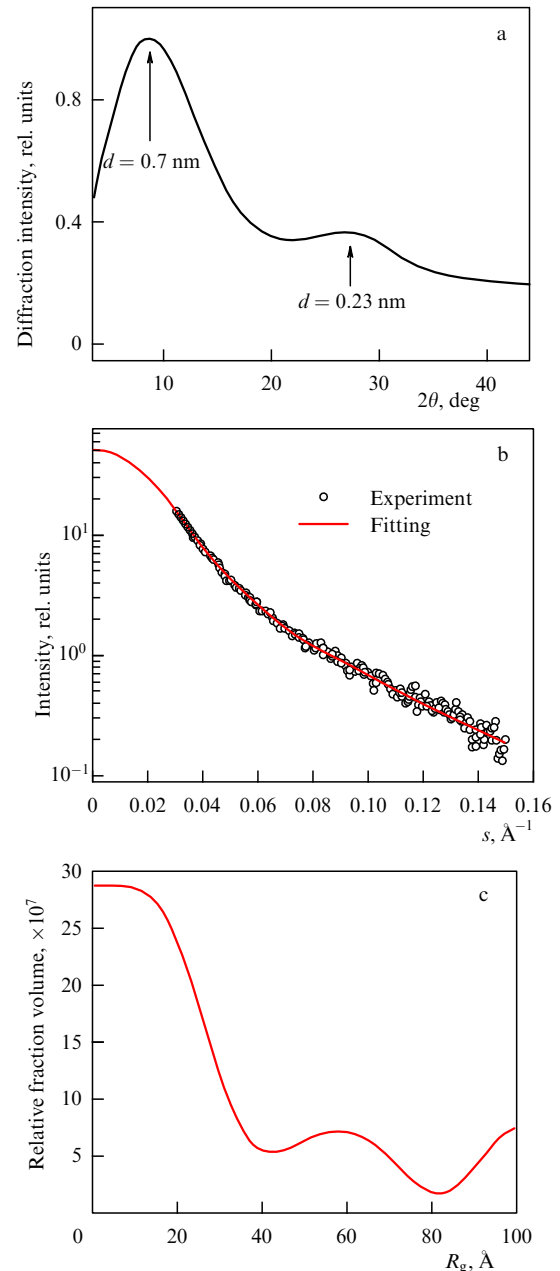


Figure 8. Diffraction spectra: (a) X-ray diffraction spectrum for smooth films from the T-10 tokamak; (b) SAXS spectrum of the films, and (c) relative contribution from balls with different radii to small-angle scattering (in the framework of model representation of the scattering centers as solid balls).

and corresponds to the regular packing of graphene layers, is observed for an interplanar spacing $d_{002} = 0.335-0.345$ nm for graphene layers with regular packing, while the principal line corresponds to the planar hexagonal structure with a characteristic dimension $d_{100} = 0.214$ nm. The positions of diffraction structures observed in the experiment are far from these values. Therefore, the carbon films from the tokamak are greatly different from the graphite ones. It is reasonable to assume that the revealed diffraction components with $d = 0.23$ and 0.7 nm correlate with the characteristic dimension inherent in the weakly ordered structure of the films. These figures may be compared with such structural elements as the benzene ring sp^2 C = C 0.28 nm in size, and the fullerene C_{60} molecule 0.71 nm in diameter, as shown in the

upper left part of Fig. 14 (see Section 3.4). The presence of aromatic (benzene) and olefinic (linear) sp^2 CH structures in the films is indicated by their IR spectra, whereas the luminescence excitation spectra of the films, which are due to their electronic structure and the occurrence of radiative transitions, exhibit a certain similarity with those of the C_{60} fullerene, as shown below (Fig. 10b).

Figure 8b displays, on a semilog scale, the SAXS spectrum of the goldish film in the momentum transfer range $s = 4\pi \sin \theta / \lambda = 0.03\text{--}0.15 \text{ \AA}^{-1}$ at angle θ . An important feature of the scattering curve $I(s)$ is the absence of an interval of s values, wherein the well-known Porod law $I(s) \sim s^{-4}$ is fulfilled; this law defines the asymptotic behavior of scattering from a smooth surface of particles with a linear dimension R_g for $s \gg R_g^{-1}$. The behavior of $I(s)$ is evidence that the film contains variously sized particles (of material or nanopores) — from small, which contribute to the scattering for large s , to coarse, which define the scattering for small s . Indeed, the slope of the $I(s)$ curve represented on a log–log scale, $\Delta(\ln I) / \Delta(\ln s) = -2.66$, testifies to the rough boundaries of the scattering domains: Porod's law for scattering balls holds true with a slope equal to -4 , and for disks the slope is -2 . Therefore, the representation of this scattering curve as the size distribution of solid balls with radii R_g , according to the Guinier law $I(s) = I_0^* \exp(-s^2 R_g^2 / 3)$, is rather conventional. From the curve in Fig. 8c, which shows the distribution of the relative contributions to the scattering intensity (Fig. 8b) from the scattering centers in the form of solid balls with different radii R_g (Porod's solid ball model), one can see that there are structure nonuniformities with characteristic dimensions (conventionally speaking, diameters) of about 4 nm and 12 nm.

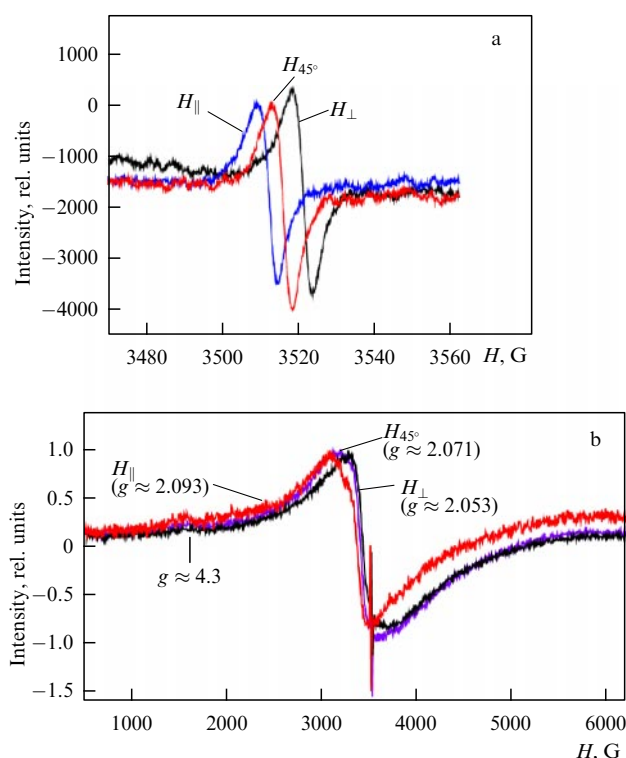


Figure 9. EPR spectra: (a) in a magnetic 100-G field, which are related to sp^2 C nanoclusters, and (b) in a 6000-G field, which are due to metal microimpurities. The spectra were obtained for three field orientations relative to the film surface.

It turns out that the 4-nm-sized structural nonuniformity correlates with experimental data obtained from EPR (100 G) data and thermal desorption spectroscopy data, which will be considered below. In particular, Fig. 9a demonstrates the EPR spectra (9.9 GHz, 100 G, 300 K) of goldish films for three orientations of a magnetic field relative to the film surface: perpendicular (H_\perp), parallel (H_\parallel), and at an angle of 45° (H_{45°), which were taken in Ref. [28].

As recently determined for a-C:H polymer films bearing a certain similarity to smooth films with a high content of hydrogen isotopes from the tokamak, paramagnetic defects with unpaired spins, which are detected with the help of EPR (100 G) spectroscopy, are related to sp^2 C nanoclusters consisting of planar aromatic rings (the ring size is about 0.28 nm), rather than to dangling σ bonds in the sp^3 (C–C) matrix (the C–C distance is about 0.145 nm), as was believed earlier: the σ bonds would relax into a planar sp^2 configuration [29]. Thanks to experimental and theoretical work over the last 20–30 years, a considerable data base has been laid for the carbon a-C and a-C:H films, and therefore we mention here only a few points. It is well known that the formation of sp^2 clusters, primarily with an even number of orbitals, leads to an energy gain and an increase in binding energy, i.e., to the stability of a cluster with delocalized π electrons, unlike the formation of a random distribution of the sp^2 and sp^3 structures. According to the widespread cluster model of a-C:H films, their electronic structure is determined by the aromatic sp^2 rings, which are bound with the help of π electrons to planar clusters of a certain size and are embedded in the sp^3 matrix. In this case, the sp^2 system, whose π electrons reside in a domain lying approximately 6 eV below the Fermi level E_F , determines the electronic properties of the system and the optical gap, while the sp^3 matrix is responsible for mechanical properties. Therefore, the cluster model is due to the occurrence of the weak and long-range attraction of the ensemble of π electrons. Defect states located inside the gap near E_F may either be empty or occupied by one or two electrons, i.e., they become paramagnetic when filled with one electron.

The EPR lines shown in Fig. 9a had the following g -factor values: $g_\parallel = 2.00348 \pm 0.00010$, $g_{45^\circ} = 2.00340$, and $g_\perp = 2.00338$. In this case, the anisotropy between the H_\parallel and H_\perp lines was 9 G, which exceeds the 6-G linewidth; in other words, it is far greater than the magnitude of anisotropy caused by the action of an internal demagnetizing field which depends on the specimen geometry, with internal anisotropy missing only from spherical specimens. Therefore, the small g -factor anisotropy for EPR (100 G) spectra, discovered in the film, may be caused by the anisotropic spatial orientation of unpaired spins in sp^2 nanoclusters.

For the EPR (9.9 GHz, 6000 G, 300 K) spectra mentioned above [25], Fig. 9b shows wide high-intensity lines with the following g -factor values: $g = 2.0534\text{--}2.0930 (\pm 0.0002)$ for three directions of the magnetic field (parallel, perpendicular, and at an angle of 45° to the film surface), which corresponds to Fe^{3+} ions in the symmetric orthorhombic state (i.e., in the film volume). The second, weak, line with $g \approx 4.3$ ($S = 5/2$) is appropriate to Fe^{3+} ions in a strongly distorted orthorhombic state (i.e., on the film surface or in pores). In this case, the magnitude of anisotropy (≈ 200 G), unlike that in the EPR spectrum taken with the 100-G field, does not exceed the linewidth (400 G).

The density of defects with unpaired spins was $n_s \sim 2 \times 10^{19} \text{ cm}^{-3}$ for sp^2 nanoclusters for EPR in the 100-G

field. Assuming their isotropic distribution over the bulk of the film, this corresponds to an average nanocluster separation of about 4 nm.

Furthermore, one can see from Fig. 9a that the effect of conduction electrons is absent. This effect may be responsible for a large anisotropy, as is the case with crystalline graphite for which $g_{\parallel} = 2.0028$ and $g_{\perp} = 2.0400$, or with polycrystalline graphite with the average value of $g = 2.0182$ [30]. In this case, the Lorentzian line shape testifies to the weakness of interaction between paramagnetic centers and to the presence of delocalized π defects, as in the case of polymer a-C:H films. As is well known, the EPR linewidth depends on the interaction between the magnetic moment of an electron and the magnetic moments of surrounding nuclei and electrons. The observed 6-G linewidth for sp^2 nanoclusters evidences the absence of appreciable spin–spin exchange interaction between the neighbors, which gives rise to line narrowing, or of dipole broadening, as in the case of the EPR (6000 G) with Fe^{3+} ion lines mentioned above, when broad lines (≈ 400 G) are due to different distances between unpaired spins and metal impurity atoms.

It should be noted that the EPR data on the films from the tokamak are somewhat different from those for polymer a-C:H films (with a high content of hydrogen), with the latter exhibiting a nearly isotropic g -factor lying in the range of $g = 2.0028$ – 2.0032 for the standard frequency 9.4 GHz, and with linewidths and defect densities being rather close to ours, as follows from Ref. [29]. In addition, a finer structure of paramagnetic centers was discovered in this work in the a-C:H film for a higher-frequency EPR (94 GHz). The structure consisted of two sp^2 clusters measuring approximately 3–4 nm. Furthermore, the increase in the g -factor with increasing the sp^2 -cluster size was also determined in Ref. [31], and a value of $g = 2.0050$ was obtained for clusters 7.5 nm in size. The relative proximity of the average magnitude of the g -factor for the films from the tokamak, $g_{av} = g_{\perp} + (g_{\parallel} - g_{\perp})/3 = 2.00341$ [28], to the value of $g = 2.00300 \pm 0.00020$ from Ref. [30] is an indication that the sp^2 cluster in the films from the tokamak measures about 4 nm.

We also note that no evidence of the discovery of metal microimpurities in a-C:H films (as in the case of smooth films from tokamaks) has come to our knowledge, with the exception of the artificial introduction of impurities into an a-C:H film.

As was revealed, the paramagnetic spin concentration $n_s \sim 10^{19} \text{ cm}^{-3}$ specified above correlates with the data on photoluminescence and luminescence excitation spectra of the films from the tokamak, which are shown in Fig. 10a [32], namely, with the magnitude of the dielectric gap $E_g \approx 3 \text{ eV}$ obtained from these spectra. The correlation between n_s and E_g is known from the data available in the literature on a-C:H films [29]. As is evident from Fig. 10a, the halfwidth of the photoluminescence spectrum (for an excitation energy of 3.3 eV) is equal to 0.5 eV, which far exceeds the magnitude of $k_B T \sim 0.025 \text{ eV}$. This testifies to a strong electron–phonon interaction and to the likelihood of noticeable localization of electron–hole pairs produced in photoexcitation with an energy $\hbar\omega \geq E_g$, with subsequent electron–hole recombination. The weak overlap of the luminescence and excitation spectra, along with an appreciable Stokes shift between the excitation and luminescence peaks, namely, $3.3 - 2.9 = 0.4 \text{ eV} \gg k_B T \sim 0.025 \text{ eV}$, suggests that there is a certain probability of radiationless recombination at impurity centers inside the dielectric gap E_g ; in this instance, the probability is caused by a high concentration of defects (estimated by means of EPR), with the latter being centers of luminescence quenching. Since the excitation spectrum peaks at 3.35 eV and the high-energy luminescence edge lies at 3.2 eV, the energy gap width is $E_g \approx 3 \text{ eV}$.

All this suggests that there is an $sp^2 + sp^3$ electron system with $E_g \approx 3 \text{ eV}$. As a result, the observed photoluminescence of the films from the tokamak, like that of a-C:H films, is excitonic in nature and turns out to arise from the $C2p \pi - \pi^*$ transitions in sp^2 nanoclusters, which are luminescence centers and which also accommodate centers of luminescence quenching by defects.

A comparison of the experimentally obtained characteristics of smooth goldish films from the tokamak (the EPR linewidth equal to 6 G, the value of $E_g \approx 3 \text{ eV}$, defect concentration equals approximately 10^{19} cm^{-3} , the absence of noticeable exchange narrowing or dipole broadening of the EPR line, and the isotopic content of the film (atomic number ratios $D/C = 0.57$, and $H/C = 0.23$)) with the corresponding literature data on a-C:H films allows a conclusion that the films from the tokamak are close to wide-band a-C:H films or tetrahedral ta-C:H films with a high content of sp^3 states ($\approx 70\%$) and a fraction of sp^2 states equal to $\approx 30\%$ [28, 33, 34]. Recently, we obtained the sp^3 –to– sp^2 state ratio directly from NEXAFS spectra for the C1s edge of smooth films from

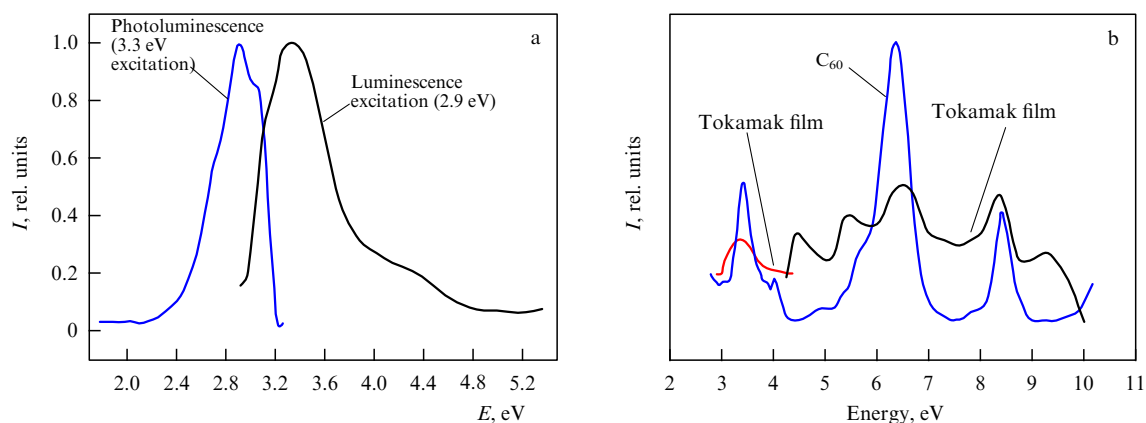


Figure 10. (a) Photoluminescence and luminescence excitation spectra of films from the tokamak. (b) Photoluminescence excitation spectra of films from the tokamak and of the C_{60} fullerene in a wide range of excitation energies (3–10 eV).

the tokamak: $sp^3 \approx 63\%$, $sp^2 \approx 37\%$, which is consistent with the previous estimates based on other experiments and literature sources.

A comparison of luminescence excitation spectra of the films from the tokamak with those of C_{60} fullerite films in a wide excitation energy range (Fig. 10b) reveals their proximity regarding several peak positions, as shown in Ref. [34]. The excitation spectra were obtained at the Sibir-2 synchrotron facility, from the D'4.2 Spekt end-station intended for the vacuum-ultraviolet (VUV) spectroscopy of solids (KCSRN) in the 200–800 nm detector sensitivity range; the low-energy part of the spectrum of the films from T-10 is the excitation spectrum depicted in Fig. 10a.

As is clear from Fig. 10b, the peaks in the excitation spectrum for the tokamak film at excitation energies of 3.34, 5.47, 6.5, and 8.43 eV are close in position to the peaks in the C_{60} film spectrum, which may respectively be attributed to the known states of $C2p$: π and mixed $\pi + \sigma$ states resided on the double $C = C$ bonds of aromatic rings, which are the structural elements common to the smooth tokamak films and to the C_{60} system. The film's spectrum peak at an excitation energy of 5.47 eV is close to the shoulder of the C_{60} spectrum peak at an energy of 5.75 eV. The higher excitation energy range, 10–13 eV, is commonly ascribed to the σ states of $C2p$; for tokamak films, they are related to the matrix with the sp^3 electronic structure for the $CH + CD$ system, while for the C_{60} system consisting of aromatic rings and pentagons with the sp^2 electronic structure, these states are related to σ bonds of pentagons. At the same time, the difference in electronic structures of C_{60} ($E_g \approx 1.8$ eV) and the tokamak films ($E_g \approx 3$ eV) should lead to a higher contribution of electronic excitations in the sp^3 subsystem for the tokamak films in the 6–10 eV energy range, as indicated in Fig. 10b. Furthermore, the sp^2 states prevail in the electronic structure of C_{60} . As is known from the literature [34], these states are more localized than the delocalized states of the carbon network in a- $C:H$ films, which manifests itself in the presence of narrower and more clearly defined peaks in the spectrum of C_{60} in Fig. 3b. Meanwhile, the dimension of a C_{60} molecule (equal to 0.71 nm in this instance) and the dimension of the aromatic ring $sp^2 C = C$ equal to 0.28 nm correlate with the X-ray diffraction data presented in Fig. 8a.

3.4 In-film hydrogen

The distributions of hydrogen in the films resulting from the co-deposition of carbon and hydrogen [24] (Fig. 11) were measured applying the nuclear recoil method with 2.2-MeV He^+ ions. These measurements showed:

(i) hydrogen in on-tungsten films is uniformly distributed over the film thickness, which suggests that hydrogen was accumulated as a result of the co-deposition of carbon and hydrogen, rather than the adsorption or introduction of bombarding ions. The co-deposition mechanism also explains the absence of saturation in the accumulation of tritium in modern tokamaks (see Fig. 1);

(ii) the hydrogen concentration in the on-tungsten film reduces as the $C_2H_2^+$ ion dose and film thickness increase, from 23.5 atomic percent (at.%) for a lower dose, when the deposited film is smooth (Fig. 7a), to 10 at.% for the highest dose, when the film exhibits a fractal structure (Fig. 7c). This is a consequence of the formation of a developed film relief, whereat it is easier for hydrogen to escape from the film;

(iii) the hydrogen concentration (see Fig. 11) near the surface of a carbon layer (curve 3) co-deposited from the

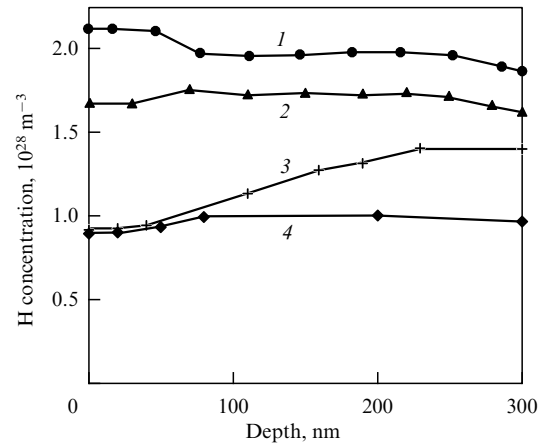


Figure 11. Depth distribution of hydrogen in the carbon layer co-deposited on tungsten substrate for different $C_2H_2^+$ ion irradiation doses: 1— $1 \times 10^{23} \text{ m}^{-2}$ (Fig. 7a), 2— $4 \times 10^{23} \text{ m}^{-2}$ (Fig. 7b), and 4— $1 \times 10^{24} \text{ m}^{-2}$ (Fig. 7c); the same on graphite: 3— $2 \times 10^{23} \text{ m}^{-2}$ (Fig. 7d).

plasma on MPG-8 graphite is in close agreement with the hydrogen concentration in an on-tungsten carbon layer with a globular structure, which develops on the entire surface irradiated with a high dose (curve 4). In this case, the concentration on the surface of the carbon layer is approximately 1.5 times lower than that at a depth of 300 nm, where it is close to the hydrogen concentration in the film formed on tungsten for an intermediate irradiation dose (curve 2).

The facts that the hydrogen concentration on the irradiated surface of the on-graphite film is lower than at greater depths and that the hydrogen concentration in the on-tungsten film reduces with an increase in irradiation dose and the formation of developed surface area are testimony to a higher-intensity desorption of hydrogen from the developed surface area.

The results of these experiments are collected in Table 1, which also gives the integral in-film hydrogen content N_H (the number of H atoms per cm^2), the film thickness d , the film density relative to the graphite density, ρ_s/ρ_0 , and the film structure.

An investigation of the D/C ratio for the films collected from different places on the divertor of the JET tokamak [13] also demonstrated that the highest D/C ratio, which amounts to 0.8–0.9, is detected in the coolest lower part of the divertor. In hotter places of the divertor, which are exposed to the plasma flux, one has $D/C = 0.1$ –0.2.

Table 1. Characteristics of the carbon layers co-deposited on tungsten and MPG-8 graphite.

Substrate material	$C_2H_2^+$ dose, m^{-2}	N_H , m^{-2}	d , μm	ρ_s/ρ_0	Film structure
W	1×10^{23}	7.2×10^{21}	1.0	0.52	Uniform (Fig. 7a)
W	4×10^{23}	5.8×10^{21}	3.3	0.79	Single globules (Fig. 7b)
W	1×10^{24}	3.2×10^{21}	10.0	0.79	Globular (Fig. 7c)
MPG-8 graphite	2×10^{23}	3.8×10^{21}			Globular (Fig. 7d)

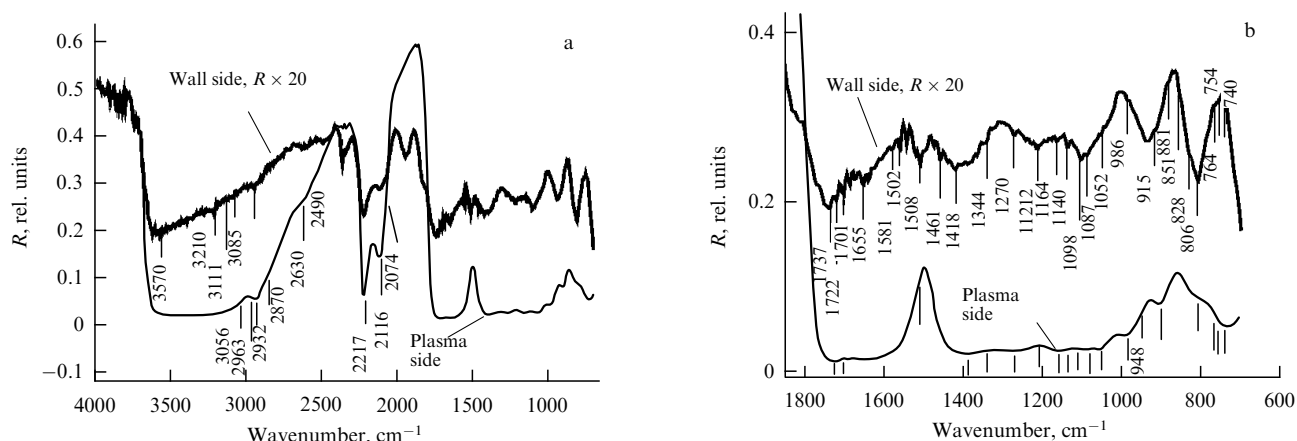


Figure 12. Infrared reflection spectra of a film from the T-10 tokamak for the plasma and wall sides of the film in the 4000–700 cm^{-1} (a) and 1800–700 cm^{-1} (b) spectral ranges.

The vibrational structure of smooth goldish films from the T-10 tokamak, which is reflective of their adsorption composition, is represented by their infrared reflection spectra (Fig. 12a) in the 4000–700 cm^{-1} frequency range, and the low-energy fragment for the 1800–700 cm^{-1} frequency range is depicted in Fig. 12b for both sides of the film: concave, i.e., facing the plasma (the plasma side), and convex, i.e., facing the wall (the wall side) [25]. For convenience of comparison, the intensity of weaker wall-side modes is multiplied by a factor of 20.

One can see that the minimum signal level for the plasma side turned out to be 2–3 times higher than for the wall side, while the maxima differ by a factor of 10–20. Furthermore, the vibrational modes of the plasma side are broader and are strongly hybridized due to their overlapping and strong absorption, which is most pronounced for the 3500–2500 cm^{-1} and 1700–700 cm^{-1} frequency intervals, while the wall side has narrower and weaker C–H, C–D, C–C, C–O, O–H modes, and some others. This difference may be explained by the presence of a surface layer with a small amount of the hydrogen isotopes H, D and the prevalence of the sp^2C states on the wall side of the film, which is clearly indicated by the weak intensity of principal deuterium modes: $\text{sp}^3\text{CD}_{2,3}$ stretching modes near the 2200–2100 cm^{-1} frequencies, as well as $\text{sp}^3\text{CH}_{1,2,3}$ stretching modes in the 2963–2870 cm^{-1} frequency interval for the wall side.

The weak modes of out-of-plane deformation aromatic sp^2CH vibrations in the 900–700 cm^{-1} frequency range are more conspicuous for the wall side. The weak deformation sp^3CD_2 modes at the frequencies of 1098, 1087, and 1052 cm^{-1} , which are observable for both sides of the film, are 3–4 times lower in intensity for the wall side. The stretching C=O modes at the 1701, 1722, and 1740 cm^{-1} frequencies are strongly hybridized for the plasma side. The aromatic stretching C–H modes at the frequency of 3056 cm^{-1} are not observed on the plasma side; however, weak aromatic stretching modes at the frequencies of 3085 and 3116 cm^{-1} manifest themselves on the wall side. A broad decrease in intensity due to saturation is observed in the domain of stretching O–H modes in the 3200–3600 cm^{-1} frequency range.

Therefore, the main difference between the IR spectra taken from both sides of the film reduces to the prevalence of aromatic sp^2 groups and the lower concentration of hydrogen isotopes, hydroxyls, and C=O groups for the wall side in

comparison with the plasma side of the film. The vibrational structure of the wall side spectrum has weaker C–C skeleton, C–H bending, and C=C–H olefinic modes and consists primarily of C–H aromatic stretching modes. Consequently, there are shorter structural portions of the carbon skeleton with weak C–H(D) modes, since the concentration of adsorbed H(D) is lower, resulting in the prevalence of the purely carbon skeleton. The structural failure of the carbon skeleton may be fostered, in addition, by the presence of atomic metal microimpurities whose concentration may be higher for the wall side.

The distinction between the two sides of the film was revealed still more clearly in the measurements of VACs for the dark current, which were taken according to the standard four-probe scheme for both sides of the film – the plasma and wall sides [25]. In particular, the presence of different charge states was established for the different sides of the film: a high-resistivity state with $\rho \approx 10^8 - 10^9 \Omega \text{ cm}$ (the plasma side), and a lower high-resistivity state with $\rho \approx 10^5 - 10^7 \Omega \text{ cm}$ (the wall side). The plasma-side VAC exhibits quasi-Ohmic behavior: the current $I \sim V^{0.9}$, i.e., the current is limited by long-lifetime charge traps. The wall-side VAC is semiconductor-like: $I \sim V^{2.3}$. Furthermore, a hysteresis is observed for the plasma side of the film, i.e., on lowering the voltage there occurs a decrease in current to a value lower than the current flowing during the increase in voltage. For the wall side, a hysteresis of the opposite type occurs. In this case, various charge states are related to different structures of defects for the opposite film sides. Specifically, the semiconductor-like VAC with the lower resistivity ρ is caused by the prevalence of the sp^2C aromatic structure and possibly by the influence of metal microimpurities, while the higher- ρ quasi-Ohmic VAC is caused by the prevalence of the sp^3C diamond structure.

This picture may be explained by considering the film formation in the tokamak. The film side facing the tokamak chamber, which has a lower resistivity and is dominated by the sp^2 carbon content, supposedly has a somewhat higher concentration of atomic metal impurities than the plasma side. This may be due to the fact that metal atoms in the co-deposition with eroding graphite particles, particularly early in the film growth on the chamber surface, have a high probability of attachment to the chamber metal surface. This is so because metal impurities have a higher sticking coefficient for a metal and the diffusion of heavy metal atoms is less probable in comparison with those for the lighter

adsorbates of hydrogen isotopes and C–H(D) groups. The plasma film side is to a greater extent exposed to bombardment by plasma particles, leading to the observed prevalence of the sp^3 structure. Subsequently, the adsorption layer being formed, whose thickness will be greater than the mean free path of the highest-energy ions and atoms, will protect the wall side of the film, in which the sp^2 structure will prevail. Metal atoms incident on the film plasma side of the adsorption layer have a higher probability of subsequent redeposition than metal atoms on the wall side.

For dark films from the T-10 tokamak with a D/C = 0.2–0.4 atomic ratio, the above-mentioned difference in VACs for the opposite sides of the film is significantly smaller, and both VACs are semiconductor-like in character, their resistivity being lower than that of the goldish films.

The aforementioned sp^3 CD_{2,3} modes in the 2200–2100 cm^{-1} frequency range, which are most intense among deuterium modes, are temperature-sensitive to the film heating and may be utilized for practical purposes for the *in situ* monitoring of the accumulation of hydrogen isotopes (deuterium and tritium) in smooth tokamak films, as well as in the cleaning of the vacuum chamber [28].

In comparison with the IR spectra of goldish films, the IR spectra of dark films [27] exhibited a lower concentration of adsorbed hydrogen isotopes and hydrocarbons, resulting primarily in the prevalence of the carbon skeleton in the dark films. The dark films have a weaker-bound, fragile structure of adsorbates with a weak C–H hybridization and short fragments of the carbon skeleton. The spectrum is mostly made up of C–H aromatic stretching modes. The stretching CD_{2,3} modes near the 2200–2100 cm^{-1} frequency range turned out to be most intense, although their intensity was somewhat weaker than for the goldish films. These modes do not correlate in intensity with the very weak modes of the carbon skeleton, but they are indicative of the presence of CD₂ and CD₃ end fragments attached to the disordered carbon skeleton.

The aforementioned adsorption of hydrogen isotopes and hydrocarbons, which results in the formation of smooth films in the tokamak, was investigated using the method of thermodesorptive Knudsen mass spectroscopy by Svechnikov et al. [27], who also measured, inter alia, some parameters of the film structure, which correlate with those indicated in Fig. 8a.

The H₂ and D₂ thermal desorption (TD) spectra for goldish films, which were obtained for a constant heating rate of 10 K min^{−1} (Fig. 13), comprise two groups of peaks: a broad group in the 450–800 K temperature range, and a narrow one at about $T = 900$ –1000 K (peaking at a temperature of about 970 K), with a higher intensity for deuterium. Both groups of peaks exhibit a fine structure; the analysis also revealed [27] that a small isotope shift (of about 6 K in magnitude for the group in the 450–800 K temperature range, and about 3 K for the group in the 900–1000 K temperature range, which is determined by the energy difference between H₂ and D₂ zero vibrations) is observed between the mutually correlating elements of the fine structure in the H₂ and D₂ spectra. These spectra turned out to be close to the TD spectra of nanographite which was obtained by milling in a ball grinder over a long period of time in an atmosphere of H₂(D₂) until reaching a crystallite size of less than 4 nm, according to Orimo et al. [35], for the same 10 K min^{−1} heating rate; the deuterium TD spectrum from that study is also given in Fig. 13. Two groups of peaks are

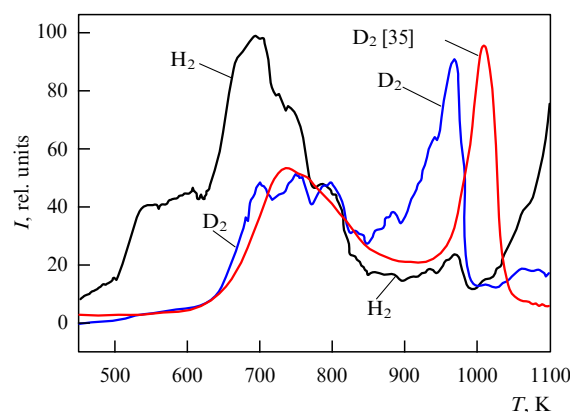


Figure 13. H₂ and D₂ thermal desorption spectra of the films from the tokamak, as well as D₂ thermal desorption spectra from Ref. [35] taken for a heating rate of 10 K min^{−1}.

seen for D₂; in this case, the first group of peaks centered at about $T = 750$ K nearly coincide with each other, while the peaks at about $T = 1000$ K are shifted relative to each other by 40 K. Such a spectral proximity, as well as the proximity of Raman spectra for these two cases, also testify to the similarity of thermal desorption processes. This permitted employing the data of Refs [35, 36] on the activation energy of H₂ desorption for interpreting the spectra in work [27].

The reason for the emergence of a narrow desorption peak near $T = 970$ K was elucidated using the following H₂ thermal desorption model. In the film formation, the fragments with neighboring C–H bonds appear at free valences of carbon. On heating to $T \approx 970$ K, two neighboring vibrating C–H bonds disrupt, resulting in the rapid formation of the H₂ molecule and its thermal desorption. This TD model proceeds from the occurrence of ruptures of existing chemical bonds due to vibrational C–H, C–D excitations and the formation of new chemical bonds, i.e., it describes a resonance type process. This feature of molecular desorption shows up in an ensemble of narrow TD peaks near $T = 970$ K (as distinct from the group of broad peaks near $T \approx 700$ K). Moreover, the proposed model corresponds to first-order kinetics and yields an asymmetric shape for the TD peak, which corresponds to the observed peaks near $T = 970$ K.

Proceeding from the experimentally examined isotope shift and desorption activation energies borrowed from the literature, the energies of C–H(D) vibrational states for the narrow TD peak near $T = 970$ K were estimated, which amounted to ~ 2400 cm^{-1} for C–H bonds, and ~ 1700 cm^{-1} for C–D bonds. These magnitudes are lower than the energies of stretching C–H modes near the frequency of 2900 cm^{-1} , and the C–D modes near the frequencies of about 2200–2100 cm^{-1} , which are indicated in Fig. 12a. Therefore, the magnitude of vibrational energy of two neighboring C–H(D) bonds is quite sufficient for effective participation in the molecular desorption of the resonance type with an activation energy of about 1.25 eV per H atom in the range of $T = 900$ –1000 K.

A broad TD peak for nanostructured graphite, which is close in shape and peak position to the peaks we observed near $T = 700$ K, was attributed in Ref. [25] to the molecular diffusion of H₂ through the boundaries of crystallites with a diffusion activation energy $E_a \approx 1.3$ eV per H₂ molecule. We

ascribed the origin of low-temperature TD peaks to the mechanism of hydrogen hopping diffusion along characteristic structural elements, which are evidenced by the foregoing results of investigations. The diffusing molecule (or atom) jumps between two equivalent potential wells with a barrier height U_a , which are separated by a distance λ .

It is significant that the mechanism of $H_2(D_2)$ molecular diffusion suggested in Ref. [36], as in other works on graphite, implies the presence of the H_2 molecule in the bulk of the carbon material at normal conditions as a result of physical adsorption in micropores. H_2 adsorption occurs in many types of graphite, as well as in carbon nanotubes; in these cases, however, the H_2 molecules are observed in the Raman $H_2(D_2)$ spectra only at low temperatures and high pressures. But, neither our Raman spectra nor the available literature data on smooth films from tokamaks have evidenced the traces of physically sorbed H_2 and D_2 in the film structure, the molecules whose presence is typical of graphite and carbon nanotubes. To explain the TD in the temperature range of $T = 450\text{--}800$ K, the model under consideration was made more specific for the case of atomic jump diffusion of $H(D)$. According to the simple model, a diffusing atom jumps between two neighboring parabolic potential wells with a barrier height U_a for an in-well oscillatory particle energy ω , a distance λ between the wells, and the diffusion activation energy $E_a = U_a + \omega/2$. Next, as a result of diffusion a rapid recombination of the atoms occurs at a common defect with the formation of an $H_2(D_2)$ molecule. Estimates made proceeding from experimental data on the isotope shift and from the value of E_a , which comprises, for atomic diffusion, half the value of $E_a \approx 1.3$ eV per H_2 molecule for molecular diffusion, i.e., $E_a \approx 0.65$ eV per H atom, yield a value of $\omega \approx 308\text{ cm}^{-1} = 38$ meV for the vibrational energy of the atom. The vibrational energy obtained corresponds to a weakly bound state of atomic hydrogen, and this model differs from the above model relying on the resonance exchange mechanism involving rupture of the C–H(D) chemical bonds in the desorption of $H_2(D_2)$ molecules at $T = 970$ K. In this case, the length of jumps between the potential wells is $\lambda \approx 3.4$ nm, which correlates with the foregoing length of ~ 4 nm between sp^2 nanoclusters with unpaired spins, estimated from EPR in a 100 G field. These nanoclusters may be the site of atomic recombination with the subsequent desorption of H_2 and D_2 molecules.

Therefore, two main adsorption states were ascribed to both groups of TD peaks in the spectra. First, ascribed to the domain of $T = 450\text{--}800$ K was a weakly bound state, i.e., the state with a low vibrational energy (≈ 30 meV) of an H atom in a model adsorption potential well and with a desorption activation energy of about 0.65 eV per H atom for this well. Second, a strongly bound (chemisorbed) state with an activation energy of ≈ 1.25 eV per H atom was ascribed to the TD range of 900–1000 K. In addition, two hydrogen isotope desorption mechanisms were proposed: the jump atomic diffusion along characteristic structural elements for weakly bound states (450–800 K), and the resonance exchange mechanism for strongly bound states (900–1000 K).

It should be noted that the TD spectra of the dark films with D/C = 0.2–0.4 are structurally close to the spectra of goldish films, namely, their adsorption states exhibit similar features.

For greater clarity, the results of investigations of the smooth goldish films collected in the T-10 tokamak, which were performed using the diagnostic techniques of the

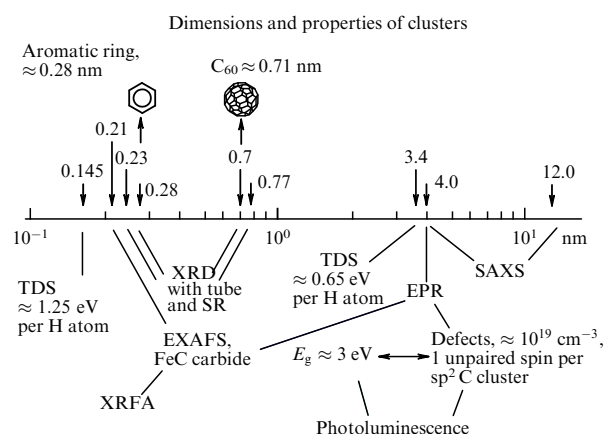


Figure 14. Schematic diagram showing the main experimental results concerning the spatial and electronic structures of the smooth films from the T-10 tokamak.

Kurchatov Center for Synchrotron Radiation and Nanotechnology (KCSRNT) at RRC KI, are represented in the form of a diagram in Fig. 14. The geometrical dimensions of the observed structural elements are indicated on the abscissa axis plotted on a logarithmic scale in the 0.1–12 nm interval. The investigation techniques are labeled below the horizontal axis; labeled above the axis are the structural elements of the known carbon nanosystems that are most close in parameters to the films from the tokamak.

The main results of investigations of the smooth films and the in-film hydrogen by the KCSRNT diagnostic techniques are as follows.

(1) The structure of smooth CH_x films is amorphous, substantially differs from the graphite structure, and contains clusters (structural defects) measuring 0.23 nm, 0.7 nm, ~ 4 nm, and 12 nm.

(2) Smooth hydrocarbon films have the property of effectively accumulating hydrogen isotopes, including D and T involved in thermonuclear reactions, which may complicate the realization of the ITER project. The D/C ratio is equal to 0.2–0.4 in smooth dark CH_x films, and to 0.5–0.9 in goldish CH_x films.

(3) The smooth films from the tokamak are close in electronic structure to wide-band a-C:H films or to tetrahedral a-C:H films with a high content ($\approx 70\%$) of sp^3 states and an sp^2 state fraction of $\approx 30\%$. At the same time, the smooth films from the tokamak have a wider dielectric gap (3 eV) than the a-C:H films (1.8 eV) formed under low-temperature plasma conditions.

(4) There are certain distinctions between the smooth films from the tokamak and the a-C:H films formed under low-temperature plasma conditions, specifically:

— the occurrence of microimpurities in smooth goldish films, primarily of transition d-metals Fe, Mo, Cr, Ni, Ti, and some others, with a total concentration of 1.5%, almost half of them being due to Fe atoms, which form an in-film Me–C cluster structure with a Fe–C separation of 0.211 nm and a coordination number of 6.2. The presence of Fe^{3+} ions was also recorded in EPR lines in the 6000 G field. The majority of microimpurities emerge in the erosion of the vacuum chamber surface (stainless steel);

— the existence of a small anisotropy in the orientation of unpaired electron spins for sp^2 C nanoclusters (for EPR in the 100 G field) in smooth goldish films;

— the difference in adsorbate properties for the two sides of goldish film, which was revealed by means of vibrational IR spectroscopy and by measuring volt-ampere characteristics. In particular, the wall side of the film exhibits a semiconductor-like VAC with a lower resistivity ρ . This VAC is due to the prevalence of an aromatic sp^2C structure and a lower concentration of adsorbates consisting of hydrogen isotopes, hydrocarbons, hydroxyls, and $C=O$ groups, as well as due to the structural failure of the carbon network arising from the possible effect of metal microimpurities in the course of the film deposition, whose concentration may be higher on the wall side. The plasma side of the film has a higher ρ with a quasi-Ohmic VAC related to the prevalence of the sp^3C diamond structure and a higher density of adsorbates. This is due to the fact that it is to a greater extent exposed to bombardment by plasma particles which disrupt the aromatic sp^2C structure and foster the formation of the sp^3C structure. This also gives rise to different types of charge traps on the opposite sides of the film, which are related to defect states, with the latter also serving as adsorption centers for hydrogen isotopes, hydrocarbons, etc.

(5) The deuterium vibrational $sp^3CD_{2,3}$ modes near the $2200\text{--}2100\text{ cm}^{-1}$ frequency range, which ‘sense’ temperature variations on film heating, may be used for practical purposes in the *in situ* monitoring of the accumulation of hydrogen isotopes (deuterium and tritium) in smooth tokamak films and in vacuum chamber cleaning.

(6) The infrared spectra of dark films are indicative of a weaker, fragile structure of adsorbates with a weak $C\text{--}H$ hybridization, of the presence of short fragments of the carbon skeleton, and of the prevalence of aromatic $C\text{--}H$ stretching modes. The difference between the VACs taken on the opposite sides of the film is appreciably smaller in the dark films. The VACs of both sides are semiconductor-like in character and have a lower resistivity compared with goldish films.

(7) In a molecular form, D_2 and H_2 were not found in the smooth films (the corresponding peaks are missing from the Raman spectra of the films).

(8) Two main adsorption states were revealed for hydrogen isotopes in smooth goldish films: a weakly bound state with an activation energy of $\approx 0.65\text{ eV}$ per H atom, and a strongly bound (chemisorbed) state with an activation energy of $\approx 1.25\text{ eV}$ per H atom. Two thermal desorption mechanisms were proposed: jump diffusion model for the weakly bound states, and the resonance exchange mechanism for the strongly bound ones. The thermal desorption spectra of the dark films are structurally close to the spectra of goldish films, i.e., their adsorption states exhibit similar features.

3.5 Theory of deposited-film relief formation

The majority of researchers believe that the eroded material is deposited in the form of atoms or ions. The fraction of dust particles is relatively small. The task of the consistent theory is to explain the relief and structure of deposited films in relation to the deposition regime, specifically, to elucidate when smooth films are formed, and when fractal ones are.

There are two main approaches to explain the formation of fractal film structures. The first implies that the fractal structure growth results directly from the deposition and attachment of atoms to a surface. The elaboration of this approach was reviewed by Budaev and Khimchenko [22]. The second approach assumes that the development of the relief structure stems from the growth of dendrites as a result of

diffusion mobility of adatoms (adsorbed atoms) over the surface (see Martynenko and Nagel’ [37]). The idea of dendrite growth on the sputtered surface, which had earlier been employed in discussing the formation mechanisms of cones and whiskers [38], turned out to be fruitful for explaining the formation of a developed relief for deposited films.

The former approach makes use of a rather clear analogy between observable cauliflower- and snowflake-like structures which grow due to diffusion-limited aggregation (DLA). The heart of this aggregation mechanism consists in the fact that the structure grows proportionally to the diffusion flux of particles depositing on its surface:

$$D \text{ grad } C, \quad (2)$$

where D is the diffusion coefficient, and C is the concentration of particles deposited near the growing surface. The growth of a smooth surface is unstable: the emergence of a protrusion of size r on a smooth surface leads to a rise in the concentration gradient in the vicinity of the protrusion:

$$\text{grad } C \sim \frac{C}{r}, \quad (3)$$

which speeds up the protrusion growth. Branching results from the growth instability of a linear protrusion. Computer simulations of this process yield structures that are indeed similar to cauliflower.

However, in the case of real fusion facilities and the corresponding model experiments, the mean free paths of atoms and ions are much longer than the characteristic structure dimensions, and the term diffusion in its ordinary sense is therefore inapplicable here. As noted in Ref. [22], the motion of atoms and ions resembles random walking owing to strong plasma turbulence. However, *the motion of ions in the near-wall plasma is not classical diffusion*. Flight trajectories of a depositing particle exist, which are rectilinear over distances exceeding the dimensions of the structure being formed. Computer simulations showed that ballistic regimes, whereat the depositing particles reach the structure surface along rectilinear trajectories, also give rise to a cauliflower-like structure. The essence of the mechanism of fractal structure growth in the ballistic regime lies in the fact that the protruding parts of the structure ‘see’ a greater solid angle of the space where the depositing atoms come from and, therefore, as in the DLA regime, grow faster. If it is assumed that the depositing atoms may diffuse some distance along the surface prior to becoming fixed, the possibilities for the simulation of the observed reliefs increase still further. However, this approach cannot explain the dependence of the film structure on the surface temperature and the fluxes of the depositing atoms and ions.

Under the last approach [37], the characteristics of deposited film relief are explained proceeding from the processes occurring initially on the surface of a substrate, and then on the surface of the coating itself, which grows due to the deposition of single atoms. The atoms deposited on the surface make up a two-dimensional gas. The concentration C of these atoms adsorbed on the surface, assuming that they are not removed from the surface (by way of evaporation or sputtering), is determined by the atomic flux q from a vacuum onto the surface, their diffusive sink, and aggregation into clusters. The aggregation of adatoms into clusters takes place due to either a fluctuation aggregation of several atoms into a

structure up to a critical nucleus in size or their attachment to impurities which serve as nucleation centers. According to the condensation theory [39], the critical size of the nucleus is given by

$$r_{cr} = \frac{2\gamma a^2}{T \ln S} = \frac{2\gamma a^2}{H - T \ln N/C}, \quad (4)$$

where $S = C/C_0$ is the supersaturation characterizing the excess of adatomic concentration over the equilibrium concentration $C_0 = N \exp(-H/k_B T)$ at a given temperature, N is the surface atomic density, H is the energy required for transferring the atom from a position in the smooth surface layer to the position of an adsorbed atom on the surface, γ is the line tension of the cluster boundary estimated as the binding energy of the nearest atoms, a is the atomic size, and T is the temperature in energy units. Clusters smaller in size than the critical one, $r < r_{cr}$, disintegrate due to adatomic detachment, while clusters with $r > r_{cr}$ grow. According to the classical theory [39], the time t_{cr} of fluctuation formation of critical-sized clusters on a clean surface is expressed as

$$t_{cr} = (DC)^{-1} \exp\left(\frac{\pi r_{cr}^2 \gamma}{aT}\right), \quad (5)$$

where D is the coefficient of adatomic diffusion over the surface, and C is the adatomic surface concentration. The fluctuation formation time t_{cr} of a critical-sized cluster lengthens with increasing temperature and supersaturation. For a low temperature and a small supersaturation, the fluctuation formation time t_{cr} of new nuclei is longer than the atomic-layer filling time

$$t_L = \frac{1}{a^2 q}, \quad (6)$$

where q is the flux of atoms depositing on the surface, and the growth of a smooth crystal surface prevails, running plane after plane. For a high T , critical nuclei have time to form and the possibility of developed relief formation emerges. This explains the fact that the developed fractal structure of the films from the T-10 tokamak was observed near the retractable limiter, which delivers the greatest amount of erosion products, especially under regimes involving limiter overheat. Away from the limiter, smooth films formed.

However, nuclei-clusters may also be formed near surface impurities. The fact that after some exposure the growth of smooth films was replaced with the formation of a developed relief in the experiments conducted by Guseva et al. [24] (see Fig. 7) testifies to the accumulation of impurity atoms on the surface. In this case, the flux of impurity atoms from the plasma is constant, and the change of regime occurs for substantially longer exposures than the time of deposition of a single atomic layer. Were the impurities delivered to the surface only from the plasma, their concentration would be constant, equal to $n_a = q_a/q$ (where q_a is the flux of impurity atoms, and q is the flux of dominant atoms onto the surface), both at the initial stage, when the growth of a smooth film is observed, and subsequently under any exposure doses. The accumulation of impurity atoms on the surface is also attested by the results of a composition analysis of redeposited tungsten films (see Fig. 7 [23]).

The accumulation of impurities on the surface may be attributed to the transfer of an impurity atom from the depths to the surface of the film with an increase in film thickness,

resulting in the accumulation of impurity atoms on the surface and the formation of a developed relief of the coating at high exposure doses.

The reason for the transfer of impurity atoms to the surface may lie with the expulsive force directed to the surface owing to a decrease in film density towards the surface, which may be due, in particular, to thermal expansion.

Impurity atoms are transferred in the direction opposite to the gradient of the diffusion coefficient D , which depends on the temperature T explicitly and implicitly due to the temperature dependence of the diffusion activation energy E_a : $D \sim \exp(-E_a(T)/T)$, so that one has

$$\begin{aligned} \text{grad } D &\sim \frac{\partial \exp(E_a/k_B T)}{\partial x} \\ &= \exp\left(-\frac{E_a}{k_B T}\right) \left(\frac{E_a}{T^2} - \frac{\partial E_a}{\partial T} \frac{1}{T}\right) \text{grad } T. \end{aligned} \quad (7)$$

The variation of diffusion activation energy E_a under temperature variations may be estimated as $\partial E_a / \partial T \approx -K\Omega\alpha$ (K is the modulus of elasticity, Ω is the atomic volume, and α is the linear expansion coefficient). Then, for a temperature

$$T > \frac{E_a}{K\Omega\alpha} \sim 1000 \text{ K},$$

the transfer of impurity atoms is directed towards higher temperatures, i.e., to the uppermost, hottest, cluster locations. Therefore, when the temperature is high enough, impurity atoms accumulate on the surface of the growing film and initiate the formation of nuclei-clusters and the consequential emergence of a developed relief.

As already noted, developed reliefs are most often represented by two types: ‘cobblestone road’ (Fig. 4b), and ‘cauliflower’ (Fig. 4c). The cobblestone road is formed when clusters grow primarily in breadth due to the attachment of adatoms to them. This takes place at moderate temperatures. At higher temperatures, a directional ‘upward’ transfer of adatoms along the relief surface prevails, also occurring to the hottest relief regions. In this case, the clusters grow primarily upwards. This is how whiskers grow [38], which are observed on sputtered high-temperature targets, along with columnar structures (Figs 5c and 5d). When a new critical-sized nucleus-cluster is formed on the surface of an upward growing column, branching of the growing branch occurs, eventually giving rise to a cauliflower-like fractal structure. This fractal structure growth is similar to the growth of a tree, wherein the transfer of ‘building material’ is due to capillary forces, which tend to transport juices to the ends of branches with the thinnest capillaries. In the case under consideration, the temperature gradient serves as the driving force.

It would be instructive to find the ranges of applicability for the model of fractal structure formation due to diffusion mobility of adatoms and the model of fractal structure formation due to deposition from the plasma volume. To do this requires comparing the atomic flux coming in to the cluster along the surface and the atomic flux going in to the cluster from the plasma volume. Such a comparison evidences that the former model is applicable to the initial stage, when the cluster separation exceeds their size, while the latter model is more adequate when the structure has already formed and the clusters are immediately adjacent to each other.

However, the on-surface adatom mobility also has its influence at the growth stage of a developed fractal structure:

it smooths the branchy fractal structure growing due to the atoms coming in from the plasma volume. Taking into account the diffusion mobility of adatoms permits determining the minimum cluster size in the fractal structure, which defines its SSA and the sorption capacity [see expression (1)].

On a surface possessing an inhomogeneity with a radius of curvature r , where there is excess pressure $P = 2\sigma/r$ (σ is the surface tension characterizing the surface energy), a flux of adatoms exists leaving the cluster due to expulsion by this pressure, as does a flux caused by the gradient of the density which is lower on the cluster. The fluxes become equal when

$$r_{\min} = \frac{2\sigma a^3}{T}, \quad (8)$$

where T is the surface temperature, and a is the atomic size. The dimension r_{\min} is precisely the minimum dimension for the existence of a cluster: for a smaller size, the cluster vanishes due to the escape of adatoms from the cluster.

For the majority of metals $\sigma a^3 \approx a$ [eV], namely, $r_{\min} \approx 15\text{--}20$ nm for $T = 500\text{--}700$ K, which agrees well with the observed minimal element of fractal structures.

3.6 Findings

(1) In tokamaks and in experiments intended to model the operating conditions in a tokamak, CH_x and W films form from erosion products; these films have either a smooth relief structure or a developed fractal one.

(2) The following tendencies were noted: smooth films are produced under low fluxes of depositing particles and low substrate temperatures, while fractal films are produced under high fluxes of depositing particles and high substrate temperatures. However, quantitative data about the formation conditions of films of various types are required.

(3) The fractal dimensionality of the films is 2.2 ± 0.2 . The specific surface area of the fractal films is defined as $\text{SSA} = 3/\rho a_0$, where ρ is the film density, and the minimum cluster size for the fractal film, $a_0 \approx 15$ nm, which corresponds to $\text{SSA}(\text{CH}_x) \approx 170 \text{ m}^2 \text{ g}^{-1}$, and $\text{SSA}(\text{W}) \approx 16 \text{ m}^2 \text{ g}^{-1}$.

(4) The structure of smooth CH_x films is amorphous, substantially differs from the structure of graphite, and contains clusters (structure defects) 0.23 nm, 0.7 nm, ≈ 4 nm, and 12 nm in size.

(5) The hydrogen content in the fractal films is relatively small: $\text{D/C} < 10\%$. In the smooth dark CH_x films, $\text{D/C} = 0.2\text{--}0.4$; in goldish CH_x films, $\text{D/C} = 0.5\text{--}0.9$.

(6) The smooth films from the tokamak are close in electronic structure to wide-band a-C:H films or to tetrahedral a-C:H films with a high content ($\approx 70\%$) of sp^3 states, and the fraction of sp^2 states coming to $\approx 30\%$. At the same time, the smooth films from the tokamak have a wider dielectric gap (3 eV) than the a-C:H films (1.8 eV) formed in low-temperature plasma conditions.

(7) Deuterium vibrational $\text{sp}^3\text{CD}_{2,3}$ modes in the $2200\text{--}2100 \text{ cm}^{-1}$ frequency range, which are temperature-sensitive to the film heating, may be employed for practical purposes for *in situ* monitoring of the accumulation of hydrogen isotopes (deuterium and tritium) in the smooth tokamak films.

(8) D_2 and H_2 were not found in a molecular form in the smooth films.

(9) Two major adsorption states of hydrogen isotopes were discovered in the smooth films: a weakly bound state with an activation energy of ≈ 0.65 eV per H atom, and a

strongly bound (chemisorbed) state with an activation energy of ≈ 1.25 eV per H atom. Two thermal desorption mechanisms were proposed: jump diffusion model for the weakly bound states, and the resonance exchange mechanism for the strongly bound ones.

(10) Hydrogen accumulation in tungsten over deposited films is poorly understood.

(11) The following film properties are also poorly understood:

(i) catalytic activity;

(ii) adhesion — the likelihood of film detachment during tokamak operation, under cleaning discharges, or when the chamber is unsealed.

4. Dust: from nano- to micrometer-scaled dust

4.1 Dust in tokamaks

Erosion in tokamaks results in the formation not only of films, but also of dust. However, dust plasma in the classical sense of the word does not form in tokamaks [40, 41]. Dust in tokamaks is accumulated on the chamber surfaces. Single dust particles rapidly vaporize on finding their way into the plasma, and therefore dust plasmas cannot be formed in tokamaks. The dust particle concentration in the plasma does not exceed $\sim 10^{-5} \text{ cm}^{-3}$ [42–44].

At the same time, dust particles affect the operation of a tokamak:

(i) when dust particles are found in the central part, they cool the plasma due to the radiation emitted by heavy impurities;

(ii) dust particles initiate blobs at the plasma periphery, enhance the particle and energy transfers to the wall, and thereby foster plasma cooling and the emergence of ELMs;

(iii) however, recently the idea has been raised of stabilizing discharge by way of dust injection.

The hazard of dust when opening the reactor chamber consists in its fugacity, the content of tritium, radioactivity, and possible toxicity, as with beryllium dust.

The main source of dust is corpuscular erosion due to emergence of ELMs and plasma disruptions. However, dust particles may be produced in the exfoliation of the films. Dust accumulates primarily on the bottom of the vacuum chamber.

Use is made of different ways to collect dust in tokamaks for conducting research. The simplest method of collecting the dust [45, 46] is to clean the tokamak chamber, either manually or with vacuum cleaners. Filters are employed to gain information about dust particle dimensions. In more accurate methods of collecting dust, advantage is taken of special dust collectors in the form of plates (most often silicon) or fibrous filters (basaltic, glass fibrous, quartz fiber, and in the form of a copper mesh), which are subsequently studied with optical or electron microscopes [16].

As the methods of dust investigation have improved, data have emerged about progressively smaller dust dispersion. Specifically, initial research using an optical or scanning electron microscope (SEM) revealed only dust particles greater than 1 μm in size. A study of thin basaltic filter layers with settled dust particles, which was performed using a transmission electron microscope (TEM), revealed dust particles of sizes down to 10 nm (Fig. 15).

The dust collected in tokamaks is characterized by Gaussian particle size distribution or by a decaying power-law distribution function with an exponent close to 2.2. The

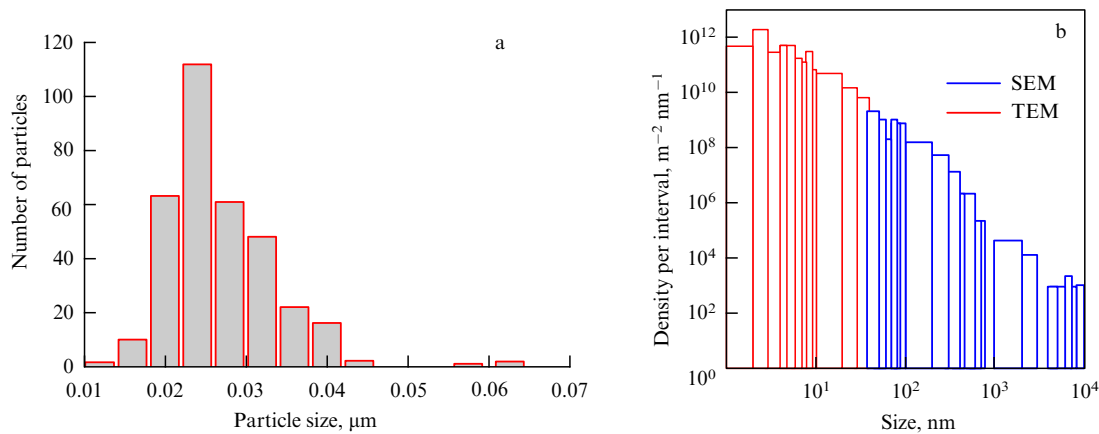


Figure 15. Size distribution of dust particles: (a) the dust collected in the T-10 tokamak, and (b) the dust collected in the Japanese LHD stellarator [47].

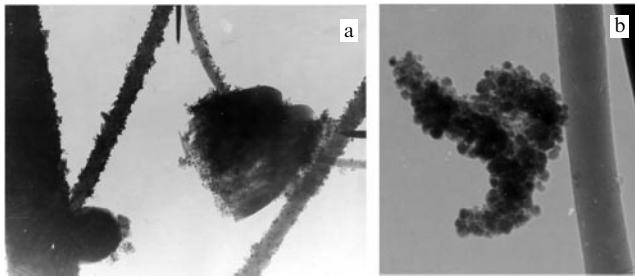


Figure 16. (a) Dust collected on a T-10 quartz filter, and (b) an agglomerate of dust particles collected in T-10.

form of the distribution depends on the place where the dust is collected and possibly on the methods of its collection and particle counting. Submicrometer-sized particles agglomerate (Fig. 16), and an agglomerate may be identified as a single particle in the particle counting. However, the majority of dust particles always have dimensions which do not exceed several dozen nanometers.

A structure analysis of large agglomerates shows that they consist of smaller agglomerates. Agglomerates may unite into larger ones; as this takes place, a fractal structure similar to the structures observed in the coatings forms.

4.2 Dust production in model experiments

Along with the collection of dust in tokamaks, the production of dust has been studied at the facilities which simulated plasma disruptions and ELMs in tokamaks. The erosion of graphite under the action of a plasma flux was first investigated in an electrodynamic plasma accelerator (plasma density: $\approx 10^{15} \text{ cm}^{-3}$; pulse duration: 60 μs ; number of pulses: 10; ion energy: 1–2 keV) [48–50]. The erosion products of different sorts of graphite [CFC, RGT (Russian graphite with a content of titanium coming approximately to 7 wt.% Ti), and MPG-8] were collected on a single-crystal silicon and a basaltic filter. The erosion products were analyzed using an optical microscope, and scanning and transmission (basaltic filter) electron microscopes.

Substantial changes occurred in the graphite composite sample upon exposure to the plasma pulses: the filling graphite material was strongly cracked and exfoliated, but the fibrous structure remained intact. The size distribution of dust particles – CFC erosion products – has two peaks: at

0.01–0.03 μm , and at 2–4 μm . Upon exposure to the plasma pulses, RGT graphite possessing an oriented grain structure becomes striated with thin cracks and pores, while the dust particles produced during its erosion range from 1 to 10 μm in size. This demonstrates how the structure of the material interacting with the plasma affects the character of its erosion and erosion products produced.

The properties of a material and the character of its erosion also depend on the prehistory of its interaction with the plasma. Martynenko et al. [50] studied the erosion and change of the RGT surface exposed to a stationary deuterium plasma and subsequently irradiated by high-power deuterium plasma pulses in an electrodynamic plasma accelerator MKT. These experiments simulated the ITER operating conditions: the normal regime, and plasma disruptions. The exposure to the stationary plasma was carried out at the Lenta facility with a deuterium ion energy of 200 eV for a surface temperature of 700 °C, whereat erosion takes place due to physical sputtering, and for a temperature of 1100 °C, whereat radiation-enhanced sublimation occurs. The ion current density amounted to $5 \times 10^{17} \text{ cm}^{-2} \text{ s}^{-1}$, and the exposure dose was 10^{22} cm^{-2} . Upon irradiation in the stationary plasma at a temperature of 700 °C, a structure resembling a brush consisting of cones formed on the graphite surface. This structure is very resistant to thermal shocks, which is why there were no substantial surface changes upon exposure to six high-power plasma pulses.

Upon exposure to the stationary plasma at a temperature of 1100 °C, a periodic structure of the 10–30- μm -high terrace type formed on the surface of a specimen. Subsequent to pulsed irradiation, traces of cleavage and brittle fractures appeared on the surface.

The size distribution of the number of particles in all cases of pulsed irradiation has two peaks: for 0.2–0.4 μm , and for 1–2 μm . In the samples exposed to the stationary plasma at $T = 1100 \text{ °C}$, however, the number of particles is greater, and large particles ranging up to 40 μm in size were also revealed in these samples. In this case, many of these dust particles are lens-shaped, similarly to the grains observed on the surface upon applying stationary irradiation. The existence of such erosion products is evidence in favor of the brittle fracture of graphite.

The temperature $T \approx 700 \text{ °C}$ is most favorable for the growth of cones under ion irradiation, resulting in the formation of a brush-like surface structure resistant to

thermal shocks. For $T > 1000^\circ\text{C}$, radiation-enhanced sublimation occurs, which arises as a result of diffusion of interstitial atoms to the surface [51]. Interstitial atoms may also diffuse towards grain boundaries and weaken the intergrain coupling [48], which also promotes brittle fracture and erosion.

Under the action of high-power plasma fluxes, a melted layer forms on the surface of a metal, but the character of its erosion and erosion products are entirely different. Along with evaporation, droplet erosion is observed, which is due to the production of capillary waves and the development of melted layer instability. The size distribution of the droplets is narrower than the analogous distribution of the particles of graphite brittle fracture (Fig. 17). The droplet size distribution peaks at $\approx 1\ \mu\text{m}$.

The character and rate of erosion due to ELMs and plasma disruptions depend heavily on the screening of the irradiated surface by the vaporized material cloud. This problem has been much studied and it has been ascertained that only several percent of the energy of the initial plasma flux reaches the surface in the disruptions. In this case, the higher the initial flux power, the lower the energy fraction reaching the surface. A review by Hassanein and Konkashbaev [52] may be recommended for familiarizing the reader with the main results of these investigations.

Experiments by Gureev et al. [53] and Kolbasov et al. [54] showed the influence of a screening layer on the number and size distribution of particles—the erosion products. Two targets located side-by-side, one of tungsten and the other of CFC, were simultaneously irradiated by a high-power deuterium plasma flux in an electrodynamic plasma accelerator ($300\ \text{kJ m}^{-2}$ per pulse, 10 pulses). The particle size distributions are different on the irradiation of a single-material target and a target of two materials (see Fig. 17). In the latter case, the particle size distribution is narrower than with one graphite target, although both spherically shaped particles and irregularly shaped particles characteristic of graphite erosion are clearly seen among the particles. This may be explained by the evaporation of small particles in the screening plasma: this plasma is more dense in the presence of tungsten vapor and radiates more strongly than on the irradiation of graphite alone. Furthermore, the number of particles generated in the case of a compound target increases. The total number of arbitrary-sized particles settled on a

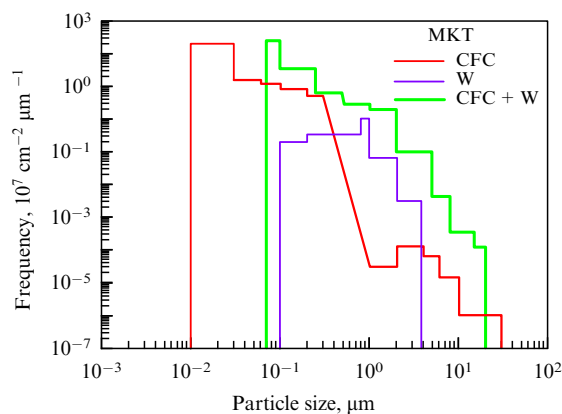


Figure 17. Particle size distribution on the irradiation of the targets made of tungsten and CFC graphite composite, and of two targets simultaneously (CFC + W) in an electrodynamic plasma accelerator.

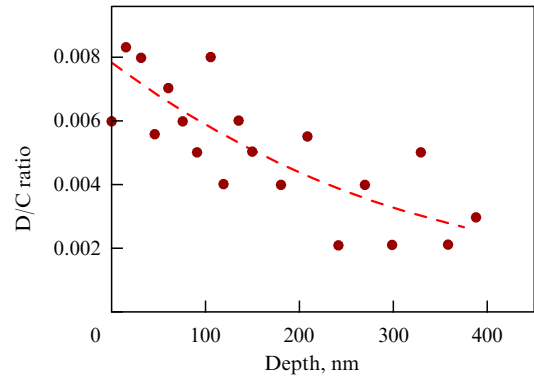


Figure 18. Deuterium distribution in a speck of graphite dust.

1-cm^2 collector area amounts to $5 \times 10^6\ \text{cm}^{-2}$ for W, $5.5 \times 10^7\ \text{cm}^{-2}$ for CFC, and $1.75 \times 10^8\ \text{cm}^{-2}$ for CFC + W.

Also of interest is the spatial distribution of outgoing particles. Guseva et al. [55] performed an experimental study of the dust products of tungsten erosion in an electrodynamic plasma accelerator. First, the erosion products were collected on a silicon detector, which entrapped droplets emanating parallel to the target surface. Second, the droplets returning to the tungsten target were also investigated. Third, the particles emanating nearly along the normal to the surface were collected on a basaltic filter.

Small droplets either return to the surface or emanate parallel to the surface. Large droplets fly off in the direction nearly normal to the surface. An explanation of this effect is provided by the theory outlined in Section 4.3.

A study of hydrogen content in the dust showed [56] that there is little hydrogen in the dust and that it is distributed near the surface of the dust particles. This is evident from Fig. 18, which shows the distribution of deuterium in a speck of graphite dust [56].

The D/C ratio on the surface of the dust particle is less than 1% and decreases with depth.

4.3 Theory of dust formation

Martynenko and Moskovkin [57] first proposed the *mechanism of graphite brittle fracture* under the action of a high-power energy flux. They proceeded from the fact that the energy released on the graphite surface was lower than the atomization energy of the layer eroded in experiments, and consequently the erosion products had to contain dust particles. Guseva et al. [48] previously showed that the reason for brittle fracturing and the emission of nano- and microparticles lay with the thermal tension between neighboring grains. Fracture occurred when the following condition was met:

$$T(\alpha_1 E_1 - \alpha_2 E_2) > \sigma_{cr}, \quad (9)$$

where α_1 , E_1 and α_2 , E_2 are the thermal expansion coefficients and compression moduli of the neighboring grains, respectively, and σ_{cr} is the ultimate strength. This estimate corresponds to the experimentally obtained magnitudes of the energy flux, whereat brittle fracturing and the emission of graphite material particles occur. Based on the brittle fracture model, Sergeev et al. [58] determined the initial velocity of the outgoing particles:

$$v_0 \approx \alpha T c \approx 10^4\ \text{cm s}^{-1}, \quad (10)$$

where c is the speed of sound. Klimov et al. [59] investigated the brittle fracture of graphite pellets in a stellarator and measured the velocity of particles flying off a pellet at $\approx 10^4 \text{ cm s}^{-1}$.

Anisotropic sorts of graphite with grains oriented in one direction show a higher resistance to brittle fracture because the difference in thermal expansion is smaller for like-oriented grains.

The droplet erosion of metals results from the melting of a surface layer. On the liquid layer, waves emerge induced by the motion of the plasma, including the plasma of the vaporized material, above the melted metal surface. An energy flux threshold exists for the onset of metal melting [60]. As the energy flux increases, a plasma forms — the vapor of evaporated material, with a flux of dense plasma emerging — of the vapor above the melted layer surface. As a result, the Helmholtz instability develops in the melted layer and waves are produced [61]. As the energy flux and the plasma-vapor density are increased still further, wave crests are torn off by the plasma wind above the surface. The plasma wind pressure is $p = \rho' U^2$, where U and ρ' are the velocity and density of the plasma above the surface, respectively. The dimension of droplets defined in this model is as follows:

$$r_1 \approx \lambda \left(\frac{v^2 \rho}{6\pi^3 \lambda \alpha} \right)^{1/4} \quad (11)$$

(λ is the wavelength, v is the coefficient of kinematic viscosity, ρ is the melted metal density, and α is the surface tension); its value approximates $1 \text{ }\mu\text{m}$, which agrees with experimental data. The initial fly-off droplet velocity parallel to the surface is given by

$$V_{\parallel} = U \left(\frac{\rho'}{2\pi\rho} \right)^{1/2} \approx 3 \times 10^2 \text{ cm s}^{-1}, \quad (12)$$

while the initial velocity normal to the surface is

$$v_0 \approx a\gamma \approx 10^3 \text{ cm s}^{-1}, \quad (13)$$

where a is the amplitude, and γ is the increment of the waves. Eventually, the fly-off droplet velocity equals

$$\mathbf{V} = \mathbf{V}_{\perp} + \mathbf{V}_{\parallel}, \quad V \approx 10^3 \text{ cm s}^{-1}.$$

4.4 Dust particles in plasma

The particle characteristics given in Section 4.3 pertain to the moment a particle departs from the eroding surface. In its transit through the plasma, including the plasma of the ionized vapor of evaporated target material, changes occur in the particle velocity and size. Near the material surface, in the Knudsen plasma layer, a directional flow of particles from the plasma to the surface shows its worth, which decelerates the departing particles. As a result, the velocity of grains lowers in transit through the Knudsen layer and becomes equal to [61]

$$v = \left(v_0^2 - \frac{1.5pl}{\rho R} \right)^{1/2}, \quad (14)$$

where $p = nT$ is the plasma pressure which decelerates the departing particles, and $l = 1/(n\sigma)$ is the thickness of this layer equal to the mean free path of electrons and ions.

Therefore, a minimum size of the grains which are capable of penetrating through this layer exists:

$$R_{\min} = \frac{1.5pl}{\rho v_0^2}. \quad (15)$$

This accounts for the prevalence of small droplets among those which returned to the specimen's surface and settled on the silicon collector, which was located near the specimen in the experiments of Martynenko et al. [50].

It should be noted that the velocity of tungsten droplets, $\sim 10^3 \text{ cm s}^{-1}$, is nearly an order of magnitude lower than the velocity of graphite particles departing due to brittle fracture. This has the result that in the course of a pulse the droplets recede from the surface by a distance of only $\approx 5 \times 10^{-2} \text{ cm}$, where the screening plasma temperature is moderate, and do not 'burn' during the action of the pulse. This underlies a better observability of tungsten droplets in comparison with that of graphite particles, for instance, at the MK-200 facility.

The particles passed through the Knudsen layer end up in the plasma and experience there the viscous friction force

$$F_t = 6\pi\eta Rv, \quad (16)$$

where η is the coefficient of dynamic viscosity. Hence, it is possible to derive the characteristic deceleration time for a dust particle and the time of its entrainment by the plasma flow:

$$t_t \approx \frac{2\rho R^2}{9}, \quad (17)$$

as well as the distance over which the particle loses its directional velocity:

$$l = v_0 t_t \approx \frac{2v_0 \rho R^2}{9}. \quad (18)$$

For a surface plasma with $T = 10 \text{ eV}$, the characteristic deceleration time for a $1 \text{ }\mu\text{m}$ -sized particle amounts to $\sim 10^{-5} - 10^{-4} \text{ s}$. During this period, the particle moves off from the surface by less than $l \approx 1 \text{ cm}$. Smaller particles are decelerated even faster and their distance to the surface is even shorter. Larger particles experience a smaller deceleration; if a particle passes the cool layer of the weakly ionized plasma near the wall during the course of the pulse, its deceleration in plasma with a high ion charge Z moderates drastically because the viscosity $\eta \sim Z^{-4}$.

Furthermore, particles vaporize in the plasma. The particle evaporation rate dr/dt may be determined from the particle balance equation

$$\frac{dr}{dt} = \frac{Q}{\rho H}, \quad (19)$$

where ρ is the particle density, and H is the sublimation energy per unit mass. Particles smaller in size than the electron and ion mean free paths in the plasma are not screened by the vapor of evaporated material. For typical parameters of plasma-vapor ($n = 10^{17} \text{ cm}^{-3}$, $T_e = 5 - 10 \text{ eV}$), the mean free path is $\lambda \approx 10^{-2} \text{ cm}$, and therefore the dust particles experience an unperturbed flux of electrons and ions. In the simplest, most frequently used approximation, the energy flux per particle is taken to be equal to

$$Q = 2T_e n_e v_e \exp\left(-\frac{e\phi}{T_e}\right) + (2T_i + e\phi) n_i v_i, \quad (20)$$

where T_e and T_i are the electron and ion temperatures, n_e and n_i are the electron and ion number densities in the plasma of the vapor of evaporated particle material, v_e and v_i are the electron and ion velocities, e is the electron charge, and φ is the particle's potential, $\varphi \approx 3.5T_e/e$. For these screening plasma parameters, the particle vaporizes with a rate $dr/dt \approx 1 \text{ cm s}^{-1}$, and the range of a graphite particle even as large as $10 \text{ }\mu\text{m}$ would not exceed several centimeters. Hence, it follows that only those particles that fly off at the periphery of the vaporized material plasma plume may reach the particle collectors. Therein lies yet another reason why in the experiments of Martynenko et al. [50] only large particles reached the collector located near the normal to the target and why their concentration was two orders of magnitude lower than the concentration of particles emanating parallel to the target surface.

An important characteristic of a particle in the plasma is its charge q , which is related to the particle's potential φ : $q = \varphi r$. It is commonly assumed [62] that the particle potential is determined by the balance of electron and ion fluxes onto the particle:

$$n_e v_e \exp\left(-\frac{e\varphi}{T_e}\right) + n_i v_i = 0. \quad (21)$$

Then, for $n_e = n_i$, one finds $e\varphi = -T_e / \ln(v_e/v_i)$.

However, recently it has become clear that the potential of a plasma particle is determined both by charged particle fluxes onto the particle and by charge fluxes from the particle [63, 64]. The charge fluxes from the particle may be caused by secondary electron [65] and ion–electron emissions, as well as by photoelectron [63] and thermal electron [65, 67, 68] emissions. Thermal electron emission is dominant for a hot particle in plasma. In this case, since the thermal electron emission depends on temperature and the temperature is determined by the balance of energy fluxes onto the particle, which in turn depend on the particle potential, the problem of determining the particle charge and temperature is to be solved self-consistently. By way of self-consistent solution to the charge–energy balance equations for a nanoparticle in plasma, Martynenko et al. [68] found its potential and equilibrium temperature T_p with the inclusion of thermal electron emission. It was shown that two stable nanoparticle states may exist in the plasma under certain plasma parameters: one state with a lower temperature and a negative potential, and the other with a higher temperature and a positive potential. The realization of one state or the other depends on the initial conditions. For a positive potential there is no barrier for electrons that arrive at the particle, and the thermal electron emission effectively heats the particle: every emission electron carries away an energy equal to the work function w , and instead an electron arrives from the plasma to bring an energy $2T_e + w$. That is why, a positively charged particle has a temperature which exceeds the temperature of ions and neutral atoms. The critical degree of plasma ionization α_{cr} , beginning from which only positive nanoparticle potentials are possible, is less than 1% for an electron temperature $T_e = 0.5 \text{ eV}$ and a vapor density $n = 10^{18} \text{ cm}^{-3}$, with α_{cr} lowering with increasing T_e and decreasing n . Hence, it follows that the condensation of vapor is impossible for the degrees of ionization actually existing in the plasma of vaporized materials, even though the vapor atoms may cool off, i.e., dust particles cannot be formed in the volume and the bulk of eroded material is deposited on the surface in the form of atoms or ions.

The agglomeration of dust particles in plasma was first theoretically considered by Boufendi and Bouchoule [69]. They assumed that negatively charged particles levitate in the electric field above the wall surface and stick together until their charge increases to the extent that Coulomb repulsion prevents the particles from sticking together. In this case, the greatest particle size was estimated at $1 \text{ }\mu\text{m}$. During levitation, the particles grow due to the deposition of atoms and ions to assume a spherical shape. The levitation terminates for some critical particle size, when gravitational forces, which are proportional to the cube of the particle size, and/or the entrainment force of ion flux, which is proportional to the square of the particle size, exceed the force, which is proportional to the particle size, experienced by the charge in the electric field of the wall. However, it remains unclear why a negatively charged particle levitates near the wall instead of drifting to the central plasma domain with a positive potential.

The agglomeration of larger particles ($\sim 10 \text{ }\mu\text{m}$) considered by Winter and Gebauer [41] implies the attraction of particles due to thermophoresis—the motion of a particle from a hot domain to a cooler one. In this case, they assumed without adducing arguments that the particle is cooler than the ambient neutral component.

The agglomeration of the dust particles levitating above the wall surface is easier to understand if it is assumed that the particle potential in the plasma is positive. Such particles are attracted to the wall with a negative potential, but when the particle approaches the wall at a distance of $\sim 1 \text{ nm}$ the tunnel current from the wall recharges the particle to the negative wall potential. After that, the particle recedes from the wall to acquire a positive charge once more, in accordance with the charge–energy balance described above, and is attracted to the wall again. Therefore, the particle oscillates about the position whereat the tunnel current onto the particle is equal to the electron current from the plasma. In this case, the change in particle charge fosters their attraction and agglomeration. The particle levitating above the surface grows due to the fluxes of ions and neutral atoms of eroding material onto the particle. The authors of Ref. [41] believed that the particle assumed a spherical shape in the course of such a growth. However, the spherical shape is realized only for a high mobility of atoms over the particle surface. Otherwise, the settling atoms are immobilized at the place where they have deposited onto the particle and a fractal structure grows. This was most clearly shown by Budaev and Khimchenko [15].

According to Ref. [41], large particles should settle onto the surface under the action of gravitational forces and the pressure of ion fluxes. The dust particles deposited onto the surface are covered by the atoms of eroding material and hydrogen isotopes. In this case, a film with strong adhesion may be formed. Under some deposition regimes, however, the dust particles remain weakly coupled to the surface and are easily mobilized in the course of tokamak operation or under cleaning discharges. The question of the amount of easily mobilized dust and the regimes of its production is important to the functioning of tokamaks and in ensuring their safe operation.

4.5 Plasma stabilization by dust injection

Of significant interest is the influence of dust on plasma behavior. Until recently, investigations were primarily made of low-temperature ‘dust’ plasmas. Considerable progress has been made in dust plasma investigations under conditions of a

laboratory high-frequency (HF) discharge, a glow DC discharge, and cosmic and radioactive plasmas [70]. However, it was shown recently that dust may play a role of no less importance in high-temperature plasmas [71–75]. In these experiments performed at a plasma-focus (PF) type pinch facility it was shown for the first time that the presence of a fraction of dust in the discharge entails a substantial improvement in magnetohydrodynamic (MHD) stability of the pinch under formation. These experiments were carried out at the PF-3 facility, which is a Filippov type PF (plane geometry of electrodes) [76]. The total capacitance of the power supply was 9.2 mF, the highest charging voltage was 25 kV, and the highest storage energy was 2.8 MJ. Actually, the case in point is a magnetic energy storage, wherein the power supply energy is converted to the magnetic energy of current at the stage of motion of the current-plasma shell (CPS) towards the discharge system axis with the subsequent current breaking and power peaking due to the development of strong current instabilities in the resultant on-axis dense pinch and the liberation of the stored energy on the plasma load.

A schematic representation of the experiment is shown in Fig. 19a. A dust target is produced on the axis of the system as a freely falling stream of finely dispersed powder. Producing a dust target with requisite parameters is a rather complicated task in and of itself. The main complexity consists in the fact that dust particles stick together to form large-sized agglomerates. To form the dust particle stream in the experiments carried out at the PF-3 facility, advantage was taken of a special device, which was located on the upper lid (cathode) of the vacuum chamber and consisted of a dust reservoir, an electromagnet, a forming flight-path tube, and a vacuum valve. On filling up, the dust source is sealed, evacuated, and then connected via a sluice valve to the discharge volume filled with the working gas (Ne, $P \approx 1\text{--}3$ Torr). For dust particles, use was primarily made of differently dispersed Al_2O_3 powder ($2\text{--}6\text{ }\mu\text{m}$ and $10\text{--}50\text{ }\mu\text{m}$). Aluminum oxide with the indicated dispersivity is characterized by a relatively low shear strength and evenly issues under gravity through a narrow conical annular slit, which opens on raising the core of the electromagnet. By varying the slit height it was possible to control the mass flow rate of the dust from the reservoir and, accordingly, the density of the dust particle stream in the region of interaction with the current shell. To form the requisite profile of the dust flow, use was made of different nozzles at the reservoir outlet and of variously shaped flight-path tubes. Subsequently, the dust stream propagated freely down to the anode surface. Under real experimental conditions, the flight-path tube was filled with the working gas at the same pressure as the working chamber, i.e., the dust particles moved through the gas medium at a pressure of several torrs along their ≈ 75 cm-long path from the dust source to the anode. The agglomerates formed in this case and large particles traverse this gap with a free-fall velocity in several tenths of a second. For particles $\sim 10\text{ }\mu\text{m}$ in size, a significant part is played by viscosity, with the result that a free-molecular fall regime sets in. According to estimates made for typical dimensions of dust particles and a working pressure of several torrs, the equilibrium fall velocity, whereat the force of gravity is balanced by the viscous force, is reached rather quickly (in several tenths of a second). In this case, the stationary (equilibrium) fall velocity u is defined by the expression [75] $u \sim 10a/P$, where a is the particle size, and P is the gas pressure.

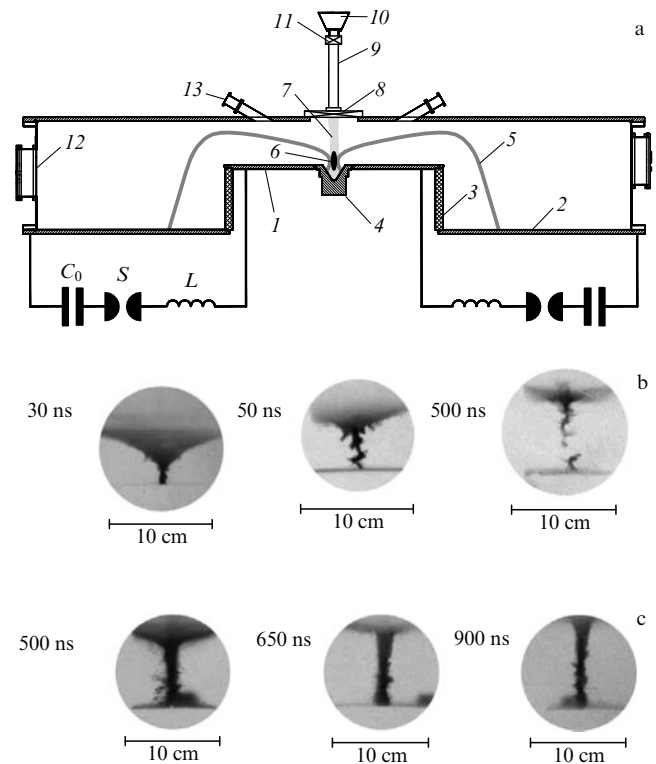


Figure 19. Experiment performed at the PF-3 facility. (a) Schematic representation of the experiment at the PF-3 facility: 1— anode, 2— cathode, 3— insulator, 4— anode insert, 5— current plasma shell, 6— pinch, 7— dust column, 8— slide valve, 9— forming flight-path tube, 10— reservoir with dust particles, 11— electromagnetic valve, 12, 13— diagnostic windows, C_0 — bank of capacitors, S — low-pressure spark gap, and L — external inductance. (b) Sequential dust-free discharge photographs. The time is reckoned from the peak in the derivative of the current. (c) Sequential photographs of a discharge with dust. The time is reckoned from the peak in the derivative of the current.

Therefore, the separation of particles according to their size occurs in the flight path. Since the total PF-discharge duration amounts to only about $10\text{ }\mu\text{s}$, the dust target may be treated as a quasistationary one in the course of the discharge. By varying the time delay between the actuation of the source valve and discharge initiation (usually several seconds), it is possible to purposefully change the parameters of the dust target interacting with the high-temperature pinch plasma.

Experiments were performed with neon as the working gas at a pressure of $1\text{--}3$ Torr and a discharge current of $2.5\text{--}2.8$ MA. The energy stored in the capacitive power supply was ≥ 500 kJ. To investigate the current-plasma shell dynamics, use was made of a four-channel nanosecond image tube (IT). Photographs were obtained perpendicular to the PF-3 chamber axis.

Referring to the images obtained using the IT, it is evident that even at the early stages of a dust-free discharge and after the highest compression the pinch is subject to different MHD instabilities which are responsible for pinch disruption (Fig. 19b). However, the on-axis plasma retains a stable shape for a long time in the case of discharges with a dense dust column. Upon axial compression of the pinch it is not disrupted and exists in a stable state for more than $1\text{ }\mu\text{s}$. Upon axial compression, the shell rises along the dust column to increase the pinch height. As a consequence, the pinch formation mechanisms may considerably alter in the pre-

sence of the dust load. In this case, it becomes possible to purposefully control their course for the solution of the task selected.

The experimental arrangement is such that the dust target ‘sees’ the current shell, which is compressed from the anode edge ($R = 46$ cm) towards the axis for a long time (≈ 10 μ s). When a high- Z gas is used, the dust particles are exposed to the high-intensity radiation from the shell even prior to direct plasma–dust contact. Estimates given by Myalton et al. [75] suggest that when use is made of, say, neon as the working gas, a plasma shell temperature of 10–15 eV would suffice to completely vaporize Al_2O_3 dust particles with a radius of 10–20 μ m. When the current-plasma shell reaches the dust target domain, the physical picture of the interaction involving dust is complicated by additional effects like momentum and energy transfer in the shock-wave interaction of the high-velocity dense plasma with the dust particles, ion sputtering, the ionization of neutral particles by electron impact, etc.

Therefore, a rather efficient evaporation and ionization of the dust particles occur due to the volume nature of the interaction of dust particles with the plasma and radiation, providing additional plasma sources in the pinch domain and ‘smoothing’ the development of MHD instabilities. The degree of stability rises upon increasing the linear mass of the target. Under the assumption that the dust particles are completely vaporized, the gas density in the pinch formation domain may exceed the initial neon density in the chamber by two orders of magnitude. Naturally, this has an effect on the CPS dynamics and the parameters of the pinch being formed. Increasing the linear number of the particles will inevitably entail a lowering of the plasma temperature.

Thus, the main factors of discharge stabilization relative to MHD instabilities are the increase in plasma density and the lowering of plasma temperature.

Recently, experiments were carried out at the ASDEX (Axially Symmetric Divertor Experiment) tokamak [77] aimed at the investigation of the influence of these factors—increasing the density and lowering the temperature of the wall plasma layer (SOL)—on discharge stabilization. For this purpose, nitrogen was admitted into the divertor. An increase in the frequency and a lowering of the amplitude of ELMs resulted, which in turn may have the effect that the ELM power density flux will be lower than the erosion threshold. Furthermore, the admission of nitrogen entailed a general discharge stabilization at the ASDEX tokamak. In this case, the increase in radiation caused by the admission of nitrogen was observed only in the divertor region.

Experiments involving dust admission were performed at the Japanese NAGDIS-II facility [78], in which a beam-plasma discharge is employed to study the interaction of plasma with materials. C_xH_y dust with diameter $d < 5$ μ m was poured from above onto a plasma cylinder.

The evaporation of the dust also resulted in a lowering of the plasma temperature. The plasma density rose insignificantly. The dust injection resulted in lowering the plasma energy flux onto the wall by 20% on average.

Therefore, the feasibility of stabilizing discharges in tokamaks by means of dust injection has already been demonstrated.

Evtikhin and Golubchikov [79] came up with the idea of a dusty divertor, in which a jet of small balls or dust had to withstand the plasma power flux. In this case, the dust, along with the divertor, would serve to moderate ELMs and stabilize discharges.

To solve divertor problems, Evtikhin et al. [80] proposed the use of capillary-porous systems (CPSs) with liquid lithium as divertor elements interacting with the plasma. In this case, vaporized lithium plays the same role as vaporized dust and weakens the action of ELMs and stabilizes discharges. As a result, the energy flux onto the divertor becomes lower. Furthermore, a solid CPS with renewable liquid lithium on its surface is radiation damage-resistant in both the normal regimes and in the presence of ELMs and disruptions. High- Z materials of the solid CPS will not find their way into the plasma, which lowers the radiative plasma cooling. Experiments with a lithium divertor at the T-11 tokamak [81, 82] showed a lowering of impurity influx into the core plasma and an improvement in the discharge parameters. In this regard, the authors of Ref. [81] assert that the splashing of liquid lithium during droplet formation would be suppressed due to the capillary forces of liquid lithium in the CPS, unlike the case of the interaction of a high-energy plasma flux with the free surface of liquid lithium in ELMs and plasma disruptions. One would even expect that the resultant lithium droplets would easily vaporize, so that the utilization of liquid lithium as a material contacting the plasma may perhaps open the way to a lowering of dust production in tokamaks.

4.6 Dust–surface interaction

During the injection of dust into a plasma, part of the particles do not have time to vaporize and find themselves on the surface of plasma-facing tokamak components. The problem of interaction between the dust particles accelerated by plasma flows or electric fields and the surfaces emerges. Of interest in this connection are the findings of Myalton et al. [75] concerning dust injection into a ‘plasma focus’, who also investigated the films formed in the deposition of dust flows on collectors.

The character of deposited films depends significantly on the density of the dust target and accordingly on the energy input per dust particle, which could be changed by varying the instant the dust admission valve was opened relative to the instant of pinch discharge. This character also depends on the position of a collector on which the film was deposited. However, in all cases the dust particles were transformed into particles of a smaller size, i.e., into nano- and micro-particles, which made up the films on the collectors.

The existence of droplet tracks on a collector arranged at an angle to the incident flux (the flow density is lower than on a collector perpendicular to the flow), and of round droplets on the collector perpendicular to the flow shows that part of the dust particles do not vaporize completely and reach the collectors in a melted form.

Upon injection of a high flux of micrometer-sized dust into the discharge, particles measuring 200 nm, which could be classified as nanoclusters formed from supersaturated vapor, were discovered along with the above droplets. Their spatial distribution was indicative of the isotropy of expanding vapor flow. An elemental analysis revealed that the composition of the deposited film corresponded to Al_2O_3 dust composition.

Upon injection of a lower dust flux into the discharge and accordingly for a higher energy input per particle, the surface density of 200-nm clusters rose nearly to the limit: to 20 particles per μm^2 . This corresponds to an almost complete packing of the surface with clusters.

The most interesting film surface structures were observed for the highest energy input per dust particle. Domains of

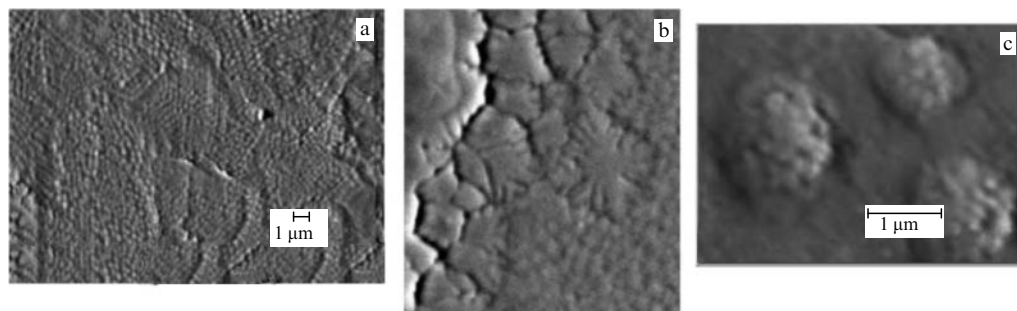


Figure 20. Structure of the films formed in the deposition of dust fluxes: (a) domains of ordered clusters which form a mesh; (b) on-film cracks in the form of snowflakes or fractal clusters, and (c) $\approx 1 \mu\text{m}$ -sized particle agglomerates comprising 200 particles of size 1 nm.

ordered clusters, which made up a mesh, formed on the surface of the collector perpendicular to the flux (Fig. 20a). As a rule, these domains formed inside the region with clearly defined boundaries. The domains measured about $5 \mu\text{m}$. The characteristic mesh pitch inside the domains was $0.5 \mu\text{m}$. The mesh could be either rectangular or circular in type. But the mesh pitch was the same in both structures. The surface cluster density was 6 clusters per μm^2 . No particles of the melt were found in these regimes: the specific energy deposition per particle was supposedly sufficient to completely vaporize the initial powder. Inside certain domains, the film surface was covered with cracks, which divided the material into cells of characteristic size $1\text{--}2 \mu\text{m}$. At the edges of the domains, the clusters limited by such cracks had the shape of snowflakes or fractal clusters (Fig. 20b). The cracks may be formed in the emergence of tensile stress in the films under cooling. The crack pattern, which is reminiscent of snowflakes, is due to the fact that the stress is removed from the greatest film surface area for a minimum overall length of the cracks, similarly to the removal of compressive stress in deposited films due to the formation of wrinkles [83].

In the highest energy input regime, round-shaped particles approximately $1 \mu\text{m}$ in diameter form on the collector arranged at an angle to the incident flux, which result from the agglomeration of smaller-diameter particles ($\approx 200 \text{ nm}$) (Fig. 20c). Similar fractal particles with a large sorption surface were also obtained in high-energy plasma discharges at the T-10 tokamak [22] and the plasma gun of a quasistationary plasma accelerator [83].

Therefore, it was shown that in all experiments involving injection of dust it was transformed into particles of smaller size, i.e., into nano- and microparticles, which made up films on the collectors. Conditions were determined whereat the dust material is deposited on collectors in the form of fractal particles, or nanoclusters, which self-organize into mesh type structures. These structures have a highly developed surface area, which is of consequence for the catalytic activity of the films and may be of significance not only for a thermonuclear reactor, but also for different technological applications.

4.7 Findings

(1) The existence of dust in tokamaks and the prevalence of a nanoparticle fraction have been established.

(2) The hydrogen content in the dust was shown to be moderate, $D/C < 1\%$.

(3) There are well-founded models of dust production.

(4) The feasibility of plasma stabilization by dust injection has been demonstrated.

(5) The dust injected into a plasma is transformed into dust particles of a smaller size and vapor, which settle on plasma-facing surfaces in the form of fractal particles, or nanoclusters, self-organizing into mesh type structures. These structures possess a strongly developed surface area.

(6) Data on the amount of dust produced are insufficient.

(7) Data on the mobilization of dust during working pulses and cleaning discharges are scarce.

5. Conclusion

The present-day outcome of investigations into nanostructures in thermonuclear facilities is an extensive database of nanostructured films and dust formed in thermonuclear facilities. Today it is known how the nanostructured films and dust are produced and where they are accumulated in tokamaks, and where deuterium and tritium are mostly accumulated.

An understanding has been gained of how to moderate or optimize the formation of nanostructured films and dust by selecting tokamak discharge regimes, choosing materials, and maybe resorting to new approaches like the use of liquid-metal or droplet walls.

The possibility of stabilizing tokamak discharges by purposeful injection of dust into tokamaks has already surfaced.

Meanwhile, such issues like hydrogen accumulation in redeposited tungsten films, the adhesion and strength of the nanostructured films, and the mobilizability of dust, as well as the chemical activity of nanostructured films, need further careful consideration.

References

1. ITER Physics Basis Editors et al. *Nucl. Fusion* **39** 2137 (1999)
2. Wesson J *Tokamaks* 2nd ed. (Oxford: Clarendon Press, 1997)
3. Federici G et al. *Nucl. Fusion* **41** 1967 (2001)
4. Bartels H-W et al. (Eds) *Accident Analysis Specifications for GSSR (AAS-3)* (Safety, Environment and Health Group, Garching ITER Joint Central Team, July, 2000)
5. Cristescu I R et al. *Nucl. Fusion* **47** S458 (2007)
6. Loarer T et al. *Nucl. Fusion* **47** 1112 (2007)
7. Kukushkin A S et al. *Nucl. Fusion* **49** 075008 (2009)
8. Koidan V S et al. *J. Nucl. Mater.* **386–388** 261 (2009)
9. Khripunov B I et al. *J. Nucl. Mater.* **390–391** 921 (2009)
10. Leonard A W et al. *Plasma Phys. Control. Fusion* **48** A149 (2006)
11. Bazylev B et al. *12th Intern. Workshop on Plasma-Facing Materials and Components for Fusion Applications*, Jülich, Germany, 11–14 May, 2009; *Phys. Scripta* **T138** 014061 (2009)
12. Guseva M I et al. *Poverkhnost: Fiz., Khim., Mekh.* (4) 97 (1986)

13. Likonen J et al. *J. Nucl. Mater.* **363**–**365** 190 (2007)
14. Alikae V V et al. *Plasma Phys. Control. Fusion* **30** 381 (1988)
15. Budaev V P, Khimchenko L N *Zh. Eksp. Teor. Fiz.* **131** 711 (2007) [*JETP* **104** 629 (2007)]
16. Romanov P V et al. *J. Nucl. Mater.* **307**–**311** 1294 (2002)
17. Ohno N et al. *J. Nucl. Mater.* **337**–**339** 35 (2005)
18. Delchambre E et al., in *Proc. 30th EPS Conf Contr. Fus. Plasma Phys. St. Petersburg, 7–11 July, 2003* ECA Vol. 27A (2003) p. 3.169
19. Rubel M et al. *Nucl. Fusion* **41** 1087 (2001)
20. Gotoh Y et al. *J. Nucl. Mater.* **313**–**316** 370 (2003)
21. Rubel M et al. *J. Nucl. Mater.* **266**–**269** 1185 (1999)
22. Budaev V P, Khimchenko L N *Physica A* **382** 359 (2007)
23. Khimchenko L N et al. *21th IAEA Fusion Conf., Chengdu, 16–21 October, 2006*
24. Guseva M I et al. *Vacuum* **67** 253 (2002)
25. Svechnikov N Yu et al. *Poverkhnost: Rentgen., Sinkhrotron. Neutron. Issled.* **12** 14 (2008) [*J. Surf. Invest. X-Ray, Synchr. Neutron. Tech.* **2** 826 (2008)]
26. Svechnikov N Yu et al. *Poverkhnost: Rentgen., Sinkhrotron. Neutron. Issled.* (1) 17 (2007) [*J. Surf. Invest. X-Ray, Synchr. Neutron Tech.* **1** 13 (2007)]
27. Svechnikov N Yu et al. *J. Nucl. Mater.* **376** 152 (2008)
28. Svechnikov N Yu et al. *Plasma Dev. Operat.* **14** 137 (2006)
29. Robertson J *Mater. Sci. Eng. R* **37** 129 (2002)
30. von Bardeleben H J *Appl. Phys. Lett.* **78** 2843 (2001)
31. Arnold G M *Carbon* **5** 33 (1967)
32. Svechnikov N Yu et al. *Voprosy Atom. Nauki Tekh. Ser. Termoyadernyi Sintez* (3) 3 (2004)
33. Svechnikov N Yu et al. *Fusion Eng. Design* **75**–**79** 339 (2005)
34. Clausing R E et al. (Eds) *Diamond and Diamond-like Films and Coatings* (NATO ASI Series., Ser. B, Vol. 286) (New York: Plenum Press, 1991)
35. Orimo S et al. *J. Appl. Phys.* **90** 1545 (2001)
36. Atsumi H, Tauchi K *J. Alloys Compounds* **356**–**357** 705 (2003)
37. Martynenko Yu V, Nagel' M Yu *Russ. Nanotekhnol.* **4** (9–10) (2009)
38. Begrambekov L B, in *Raspyslenie* (Sputtering) (Itogi Nauki i Tekhniki. Ser. Puchki Zaryazhennykh Chastits i Tverdoe Telo, Vol. 7, Ed. Yu V Martynenko) (Moscow: VINITI, 1993)
39. Frenkel J *Kineticheskaya Teoriya Zhidkosti* (Kinetic Theory of Liquids) (Leningrad: Nauka, 1975) [Translated into English (Oxford: Pergamon Press, 1946)]
40. Fortov V E et al. *Phys. Rep.* **421** 1 (2005)
41. Winter J, Gebauer G *J. Nucl. Mater.* **266**–**269** 228 (1999)
42. Krashenninnikov S I *Phys. Lett. A* **283** 368 (2001)
43. Krashenninnikov S I et al. *Phys. Plasmas* **11** 3141 (2004)
44. Krashenninnikov S I, Soboleva T K *Plasma Phys. Control. Fusion* **47** (5A) A339 (2005)
45. Carmack W J et al. “DIII-D dust particulate characterization”, Idaho National Engineering and Environmental Laboratory, IN-EEL/EXT-97-00702 (November 1997)
46. Carmack W J “DIII-D dust particulate characterization”, Idaho National Engineering and Environmental Laboratory, IN-EEL/EXT-99-00095 (January 1999)
47. Shiratani M et al., “Characterizations of dust particles ranging in size from 1 nm to over 10 μ m collected from LHD”, *Proc. 17th Plasma Surface Interactions Conf., Hefei, China, 22–26 May, 2006*
48. Guseva M I et al. *Zh. Tekh. Fiz.* **66** (6) 106 (1996) [*Tech. Phys.* **41** 578 (1996)]
49. Guseva M I et al. *Voprosy Atom. Nauki Tekh. Ser. Termoyadernyi Sintez* (1–2) 83 (1997)
50. Martynenko Yu V et al. *J. Nucl. Mater.* **258**–**263** 1120 (1998)
51. Roth J, Möller W *Nucl. Instrum. Meth. Phys. Res. B* **7**–**8** 788 (1985)
52. Hassanein A, Konkashbaev I, in *Atomic and Plasma-Material Interaction Data for Fusion* Vol. 5 (Vienna: IAEA, 1994) p. 163
53. Gureev V M et al. *Voprosy Atom. Nauki Tekh. Ser. Termoyadernyi Sintez* (1) 12 (2001)
54. Kolbasov B N et al. *Fusion Eng. Design* **54** 451 (2001)
55. Guseva M I et al. *Zh. Tekh. Fiz.* **72** (7) 48 (2002) [*Tech. Phys.* **47** 841 (2002)]
56. Martynenko Yu V, Moskovkin P G *Voprosy Atom. Nauki Tekh. Ser. Termoyadernyi Sintez* (4) 17 (1991)
57. Martynenko Yu V, Moskovkin P G *Voprosy Atom. Nauki Tekh. Ser. Termoyadernyi Sintez* (2) 31 (1999)
58. Sergeev V Yu et al. *Zh. Tekh. Fiz.* **76** (11) 66 (2006) [*Tech. Phys.* **51** 1462 (2006)]
59. Klimov N S et al. *Voprosy Atom. Nauki Tekh. Ser. Termoyadernyi Sintez* (2) 52 (2009)
60. Martynenko Yu V, Moskovkin P G *Voprosy Atom. Nauki Tekh. Ser. Termoyadernyi Sintez* (1) 65 (2000)
61. Tsytoich V N, Winter J *Usp. Fiz. Nauk* **168** 899 (1998) [*Phys. Usp.* **41** 815 (1998)]
62. Samarian A A et al. *Phys. Rev. E* **64** 056407 (2001)
63. Kozyrev A V, Shishkov A N *Pis'ma Zh. Tekh. Fiz.* **28** (12) 33 (2002) [*Tech. Phys. Lett.* **28** 504 (2002)]
64. Popel S I et al. *Fiz. Plazmy* **27** 831 (2001) [*Plasma Phys. Rep.* **27** 785 (2001)]
65. Morozov A I, Savel'ev V V *Fiz. Plazmy* **30** 330 (2004) [*Plasma Phys. Rep.* **30** 299 (2004)]
66. Smirnov B M *Usp. Fiz. Nauk* **173** 609 (2003) [*Phys. Usp.* **46** 589 (2003)]
67. Ognev L I *Pis'ma Zh. Tekh. Fiz.* **33** (22) 64 (2007) [*Tech. Phys. Lett.* **33** 972 (2007)]
68. Martynenko Yu V, Nagel' M Yu, Orlov M A *Fiz. Plazmy* **35** 542 (2009) [*Plasma Phys. Rep.* **35** 494 (2009)]
69. Boufendi L, Bouchoule A *Plasma Sources Sci. Technol.* **3** 262 (1994)
70. Fortov V E et al. *Usp. Fiz. Nauk* **174** 495 (2004) [*Phys. Usp.* **47** 447 (2004)]
71. Krauz V I et al., in *Intern. Symp. PLASMA-2001: Research and Applications of Plasmas, Warsaw, Poland, 19–21 September 2001*
72. Fortov V E et al., in *5th Int. Conf. on Z-pinches, Albuquerque, New Mexico, 23–28 June 2002; AIP Conf. Proc.* **651** 37 (2002)
73. Vinogradov V P et al. *Fiz. Plazmy* **32** 699 (2006) [*Plasma Phys. Rep.* **32** 642 (2006)]
74. Krauz V I et al. *Fiz. Plazmy* **34** 47 (2008) [*Plasma Phys. Rep.* **34** 43 (2008)]
75. Myalton V V et al., in *Intern. Symp. PLASMA-2001: Research and Applications of Plasmas, Warsaw, Poland, 19–21 September 2001*
76. Zohn H, in *22nd IAEA Fusion Energy Conf., Geneva, Switzerland, October 13, 2008, Talk OV/2-3*
77. Ohno N et al. *J. Nucl. Mater.* **390**–**391** 61 (2009)
78. Murav'ev E V *Voprosy Atom. Nauki Tekh. Ser. Termoyadernyi Sintez* ((1)7) 85 (1981)
79. Evtikhin V A, Golubchikov L G “Zhidkometallicheskiy divertor termoyadernogo reaktora-tokamaka” (“Liquid-metal divertor of a thermonuclear tokamak reactor”), Russian Federation Patent No. 2051430 (The earliest priority of February 1995)
80. Evtikhin V A et al. *Plasma Phys. Control. Fusion* **44** 955 (2002)
81. Apicella M L et al. *J. Nucl. Mater.* **363**–**365** 1346 (2007)
82. Carter G, Martynenko Yu, Moskovkin P *Thin Solid Films* **287** 275 (1996)
83. Khimchenko L et al. *Proc. 34th EPS Conf. Plasma Phys., Warsaw, Poland, 2007, O2-006*